AFRL-SR-AR-TR-05-

REPORT DOCUMENTATION PAGE

0076

1. REPORT DATE *(DD-MM-YYYY)* 15/01/05	2. REPORT TYPE Final report	3. DATES COVERED *(From - To)* June 1. 03 – August 31. 04 2004 2003

4. TITLE AND SUBTITLE	5a. CONTRACT NUMBER
DUCTILE FRACTURE OF THIN-WALLED CYLINDERS SUBJECTED TO INTENSE HEAT	
	5b. GRANT NUMBER F49620-03-1-0284
	5c. PROGRAM ELEMENT NUMBER

6. AUTHOR(S) C. T. Sun Z. Jin, S. Kalyanam, N. Bruno, A.Deitemeyer, D. Nakaima, and T. Tanner	5d. PROJECT NUMBER
	5e. TASK NUMBER
	5f. WORK UNIT NUMBER

7. PERFORMING ORGANIZATION NAME(S) AND ADDRESS(ES) Purdue University West Lafayette, Indiana 47907	8. PERFORMING ORGANIZATION REPORT NUMBER

9. SPONSORING / MONITORING AGENCY NAME(S) AND ADDRESS(ES) Air Force Office of Scientific Research 4015 Wilson Blvd., Rm 713 Arlington, VA 22203-1954 NA	10. SPONSOR/MONITOR'S ACRONYM(S)
	11. SPONSOR/MONITOR'S REPORT NUMBER(S)

12. DISTRIBUTION / AVAILABILITY STATEMENT

DISTRIBUTION UNLIMITED

13. SUPPLEMENTARY NOTES

14. ABSTRACT
The objective of this research was to further develop two models that are capable of predicting crack growth in ductile materials. In this study, we measured CTOA (crack tip opening angle) at elevated temperatures for a stainless steel and aluminum alloy 2014-T6. The CTOA curves were then used as the fracture criterion to simulate crack extension and instability in thin-walled cylinders subjected to localized intense heat. The commercial finite element code ABAQUS was used in conjunction with a user subroutine to implement the CTOA fracture criterion to perform the simulation. The result of the numerical simulations indicated that the effect of temperature on the level of burst pressure of the cylinder is not very significant. One explanation for this interesting behavior is that the heated zone that contains the crack would be subject to compressive stresses because of a greater thermal expansion. In this study, an analytical damage length (DL) model has been further developed to account for the thermal effect in addition to the large deflection effect. The DL model was also used to predict the burst pressure of steel and aluminum cylinders and the results are compared favorably with those predicted by the CTOA approach.

15. SUBJECT TERMS

16. SECURITY CLASSIFICATION OF:			17. LIMITATION OF ABSTRACT	18. NUMBER OF PAGES	19a. NAME OF RESPONSIBLE PERSON C.T. Sun
a. REPORT UNCLASSIFIED	b. ABSTRACT UNCLASSIFIED	c. THIS PAGE UNCLASSIFIED		77	19b. TELEPHONE NUMBER *(include area code)* 765-494-5130

Standard Form 298 (Rev. 8-98)
Prescribed by ANSI Std. Z39.18

Final Report

Prediction of Ductile Fracture of Thin-Walled Cylinders Subjected to Localized Intense Heat

Prepared by
C.T. Sun, Z. Jin, S. Kalyanam,
Nick Bruno, Adam Deitemeyer, Daniel Nakaima, and Travis Tanner
School of Aeronautics and Astronautics
Purdue University
West Lafayette, IN 47907

November 30, 2004

Part I Measurment of CTOA Curve

1. Equipment Adjustments/Modifications

a) Furnace Modifications

Ideally, the furnace should be adiabatic. In order to fit the specimen and the thermocouple wires into the furnace, some gaps are necessary; however, initially the furnace was not designed to fit the igniter wires which left an opening where the wires exit the furnace. In order to make the top ceramic tile flush with the rest of the furnace, four grooves were machined out of the tile. The grooves were made on the top-piece of the modified furnace.

b) Microscope Stand

Over time, the condition of the microscope stand was found to be deteriorating and inadequate. The main problems were instability and the inability to accurately re-position the microscope during testing. To fix these issues, the following modifications were made:
- The brackets holding the digital camera on the back of the microscope were re-machined in order to make them more rigid.
- C-clamps were placed on the base of the stand to restrict unintentional movement during testing.
- An angular rotation guide was applied to the transverse positioning dial in order to make transverse movement more accurate.

The end results obtained were better quality pictures, easier microscope positioning, and improved accuracy in determining crack extension.

2. Verification Test of Duplex Steel at Room Temperature

Room temperature tests were repeated on steel, to be compared with the old data. The specimens used in this test had a slightly larger crack than the ones used in the old experiments. A 26 mm crack was made using the water-jet machine. The crack was extended with a jeweler-saw on both ends of the water-jet cut. The final length of the crack after jewelers-saw cut was $2a_o=28$ mm. The specimens were further fatigue-loaded at a rate of 8Hz, using a fatigue load of 1.7-26.3 kN for 10,000 cycles. Two specimens were tested. The fatigue crack obtained for the first specimen was of length of 1.61 mm and the second specimen of length 1.51 mm.

The fracture experiment was performed at room temperature, around 25°C, under the Stroke Control mode at a rate of 0.002 mm/sec. The CTOA analysis was done using digital pictures at different crack extensions as shown in Figure 1. Figure 2 shows the new and old CTOA data which agree well. It is seen that, as the crack extends, the CTOA decreases and approaches a constant of 10°.
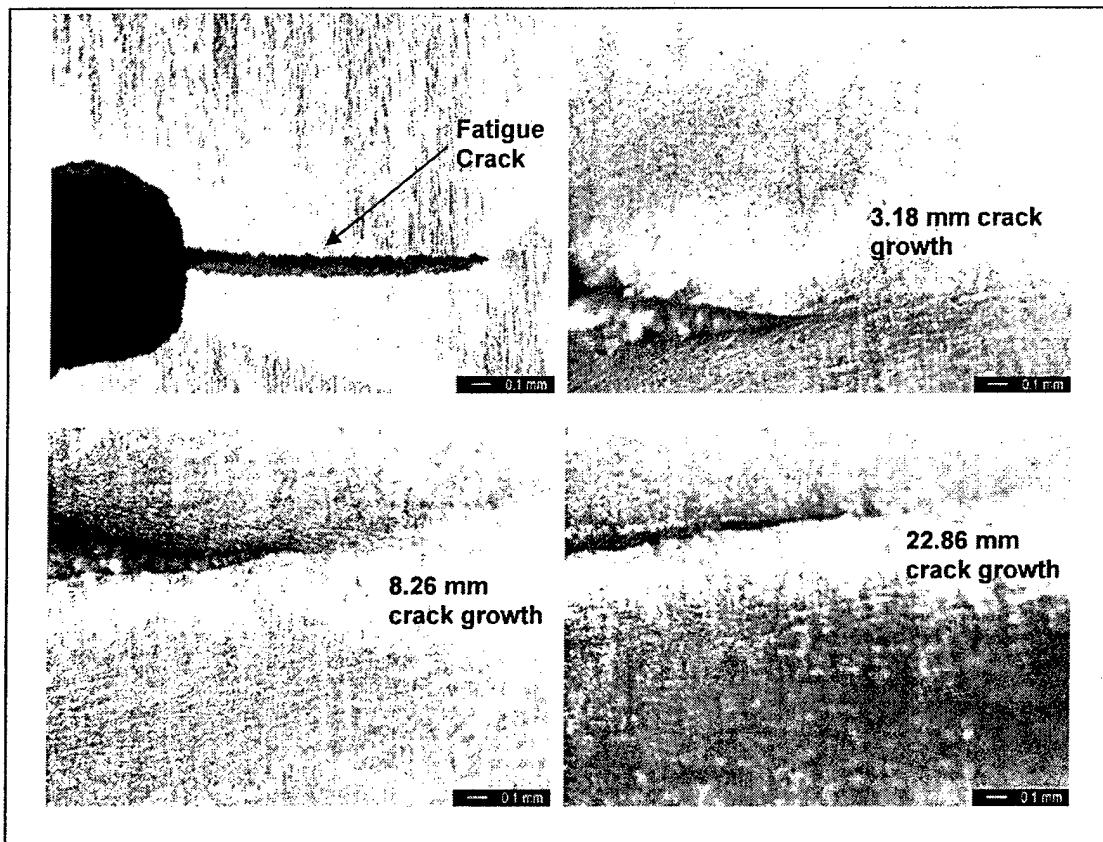

Fig.1 - Crack tip region at various stages of crack growth for steel specimens tested at room temperature.
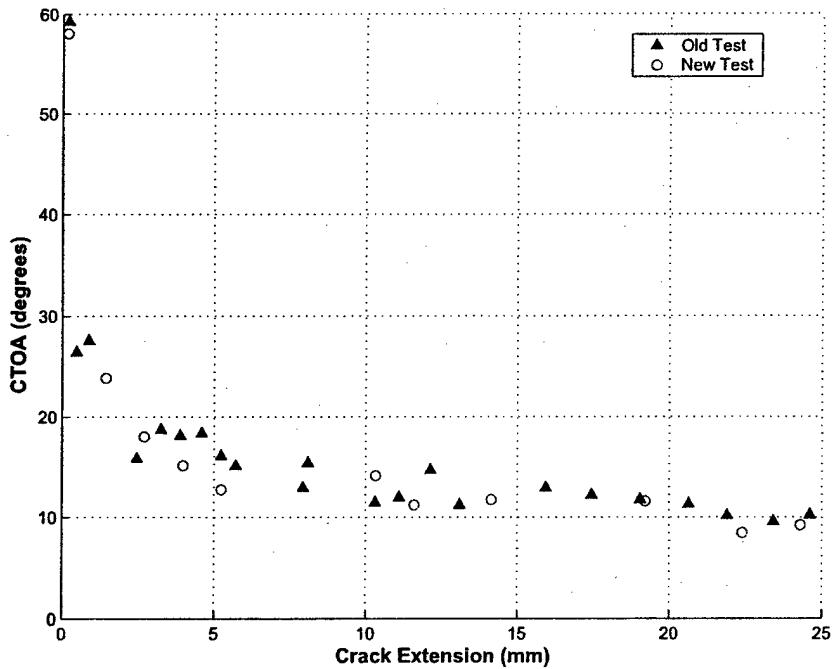
Fig. 2 CTOA variation in steel at room temperature

3. Measurement of CTOA Curves for Duplex Steel at Elevated Temperatures

a) Fracture Test of Duplex Steel at 200° C

Fracture tests were conducted on steel specimens with a center crack at 200°C. The temperature was measured by two thermocouples that are spot-welded to the surface of the metal as shown in Figure 3. The elevated temperature was attained by utilizing two igniters symmetrically located on the back wall of the heating furnace. The igniters are switched on and off to keep the temperature at the given set point. With this method the temperature stayed consistently between and 190°C to 210°C.
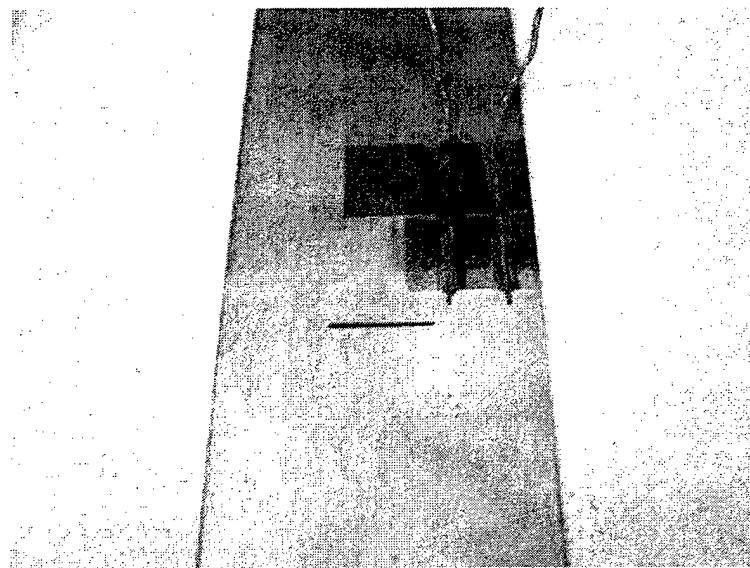
Fig. 3 Thermocouples setup.

From past fracture tests conducted on steel, the CTOA curve for specimens tested at 200°C show a lower critical CTOA value than those tested at room temperature. Due to this unexpected behavior, more fracture tests were conducted on steel specimens with a center crack at the same set point temperature. The repeated experiments followed a similar procedure as those done previously; however, the time given for the specimen to thermally reach steady state conditions was increased.

During testing, the lower part of the specimen was gripped by the hydraulic grips and heated to 200°C. The specimen is allowed to freely expand and then top part is gripped. The time allowed for the specimen to expand was approximately 15 minutes, whereas only a few minutes of expansion time were allowed in previous experiments. The tests were conducted under Stroke Control at a rate of 0.002 mm/sec.

Figure 4 shows the crack tip opening at different crack extensions. The CTOA analysis procedure was performed on the digital pictures taken at successive crack extensions. All the CTOA data are presented in Fig. 5. It is seen that, as the crack extends, the CTOA decreases until reaching a value beyond which the CTOA stays relatively constant at approximately 7°-8° degrees.
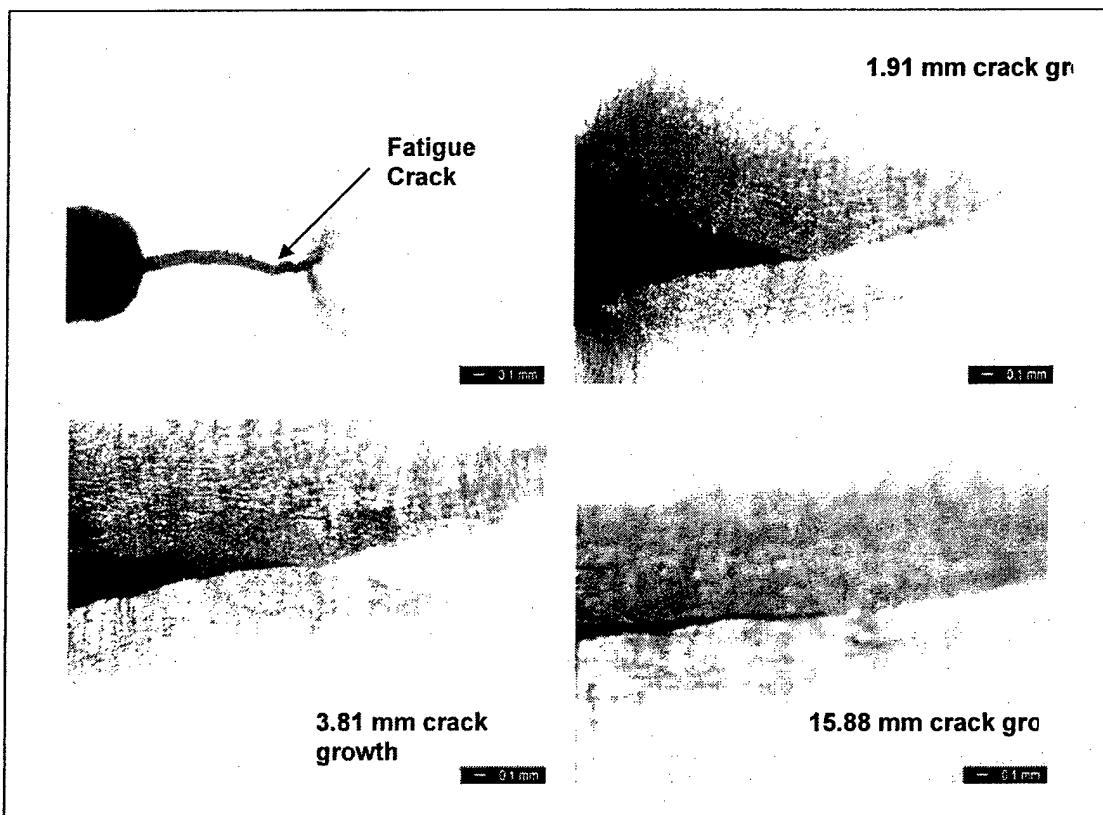
Figure 4 Crack tip region at various stages of crack growth for steel specimens tested at 200°C.
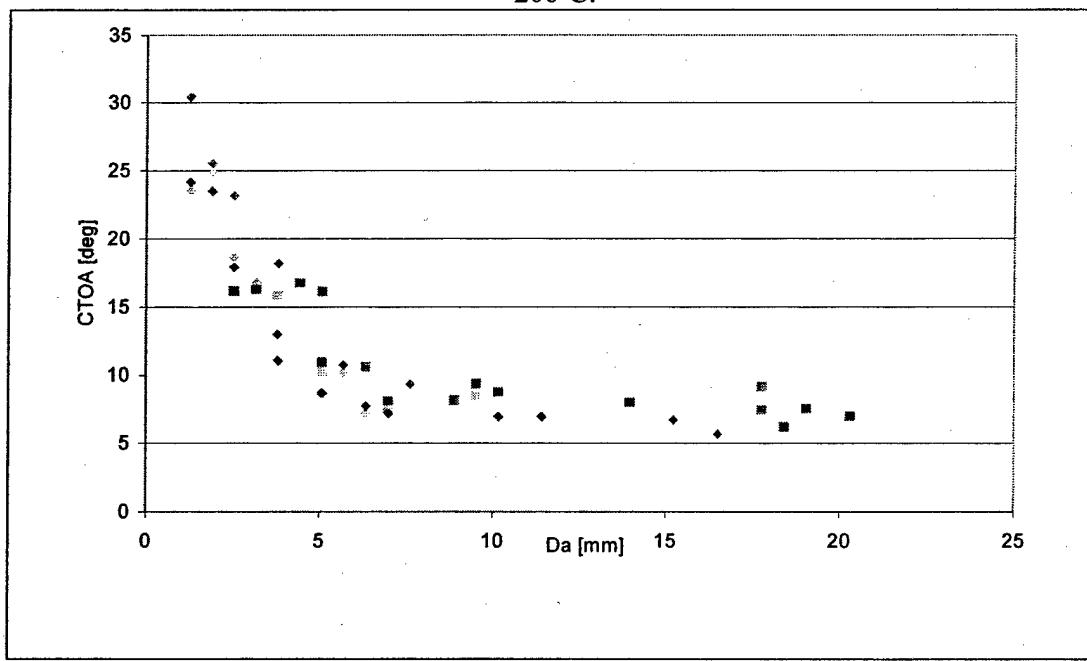

Fig. 5 CTOA curve for steel tested at 200°C.

b) Fracture Test of Duplex Steel at 400 °C

The temperature was raised to required test temperature and the test was conducted using position control at the rate of loading 0.002 *mm/sec*. The thermocouples were arranged as shown in Fig. 6. Since the required temperature was only 400 °C, the heating was obtained by attaching two heating coils at symmetric locations to the back wall of the heating furnace. A difference within 15 °C was observed between the thermocouple near the initial crack tip and the thermocouple near the edge of the specimen. Initially the thermocouple near the initial crack tip was used to control the specimen temperature. As the crack extended the temperature of the specimen was controlled by the closest thermocouple to the propagating crack tip. Fig. 7 shows the digital images captured at four different lengths of crack extension for the 400 °C test. As the crack extends the CTOA is found to decrease until a final average value close to 11° (Fig. 8).
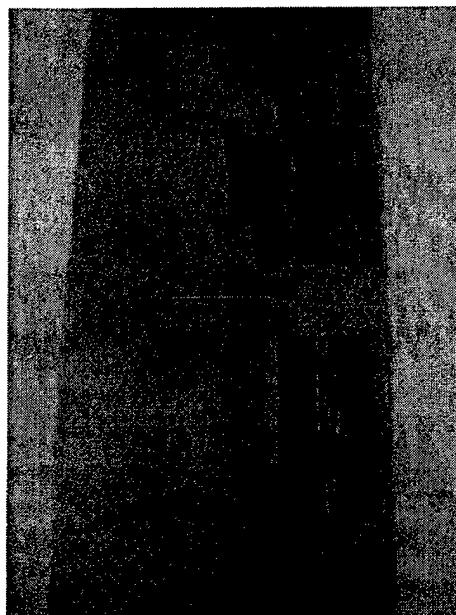

Fig. 6 Thermocouples spot welded to the center crack steel specimen
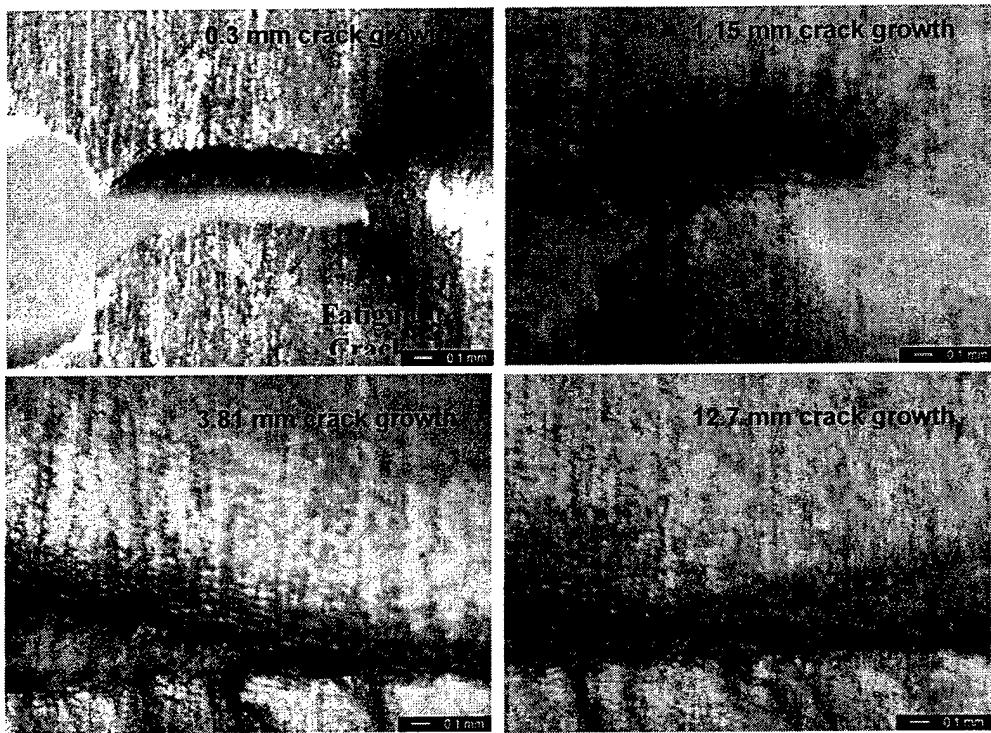
Fig. 7 Crack tip region at various stages of crack growth for steel specimens at 400 °C
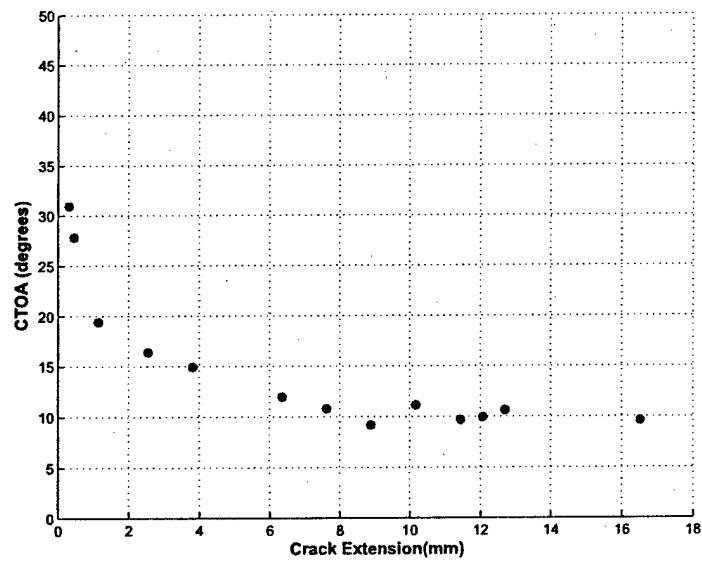
Fig. 8 CTOA variation in steel tested at 400 °C

c) Fracture Test of Duplex Steel at 600 °C

Fracture tests were conducted on center crack steel specimens earlier at 400 °C and 200 °C and two heating coils were symmetrically positioned at the back wall of the heating furnace. However to achieve a temperature of 600 °C four heating coils were required and hence additional two heating coils were placed at symmetric locations on the two side walls of the furnace. The heating coils were turned on and the temperature of the specimen was raised to the required 600 °C. The two heating coils on the side walls were turned on and off to control the temperature inside the furnace. The heating of the specimen was monitored from the measured temperatures using the three thermocouples spot-welded to the surface of the specimen as shown in Fig. 6. The temperature was controlled in the range from 590 °C to 610 °C.

The lower part of the specimen was gripped by the hydraulic grips and the specimen heated to 600 °C. It was noticed that there was considerable thermal expansion of the specimen owing to the temperature change to 600 °C. If both the ends of the specimen were gripped before heating the specimen a compressive stress would be developed during the thermal expansion of the specimen. For this reason the gripping of the top end of the specimen was done after the 600 °C temperature was reached and a few minutes allowed for the specimen to freely extend due to thermal expansion. Position controlled test was conducted at the loading rate of 0.002 mm/sec. Fig. 9 shows the digital images captured at four different lengths of crack extension. The CTOA determined from the analysis of the captured images is shown in Fig. 10. It is noticed that the CTOA decreases from the initial values around 40 degrees as the crack extends. For larger lengths of crack extension the CTOA is seen to vary mostly in the range from 22.5 to 27.5 degrees. An average value of critical CTOA of around 25 degrees can be seen from the Fig. 10 and this value is found to be much higher than the room temperature critical CTOA value of 10 degrees for large crack extensions.
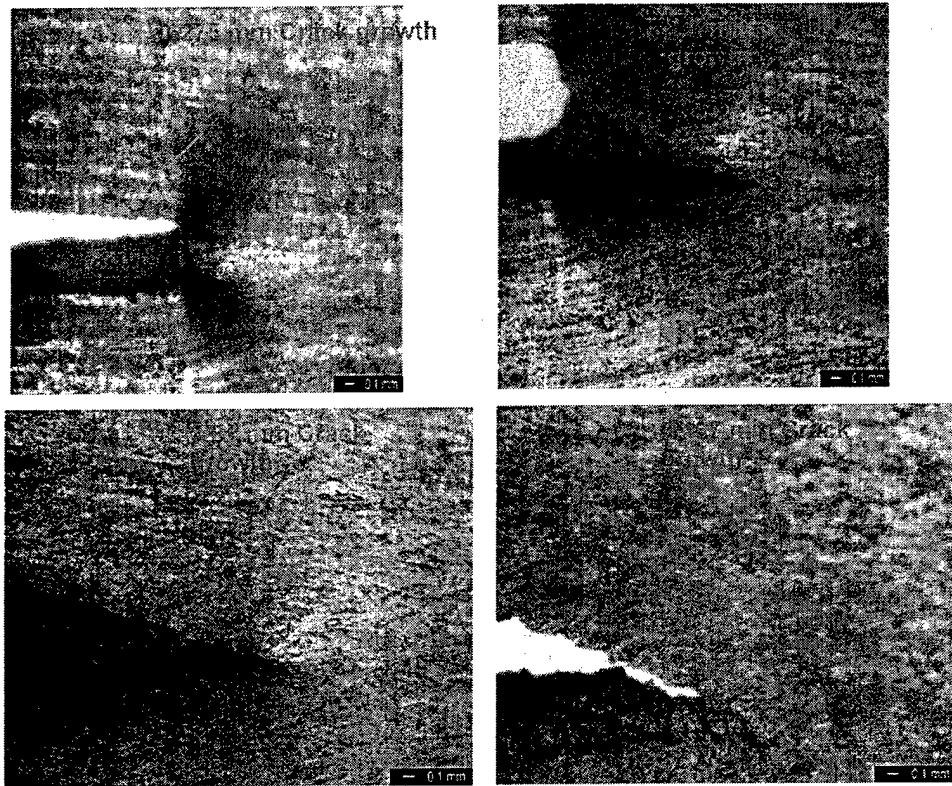
Fig. 9 Crack tip region at various stages of crack growth for steel specimens tested at 600 °C
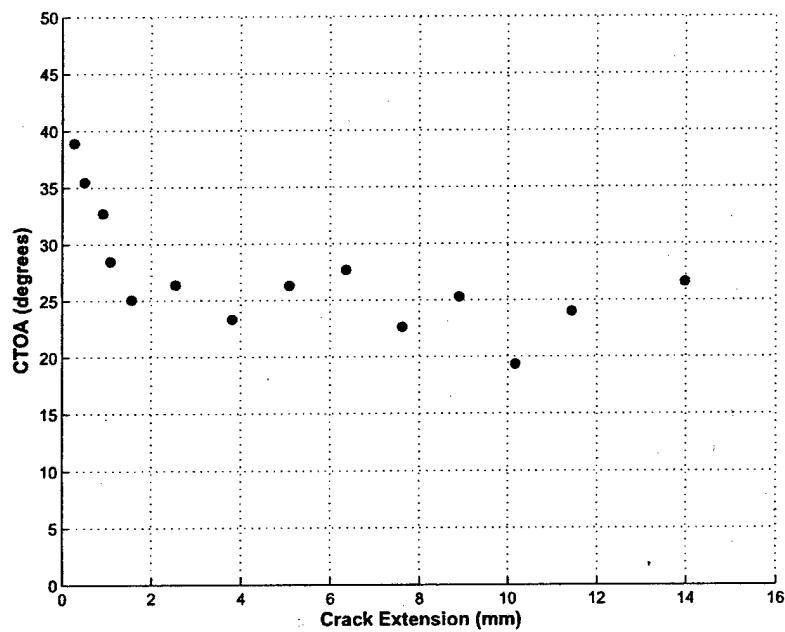

Fig. 10 CTOA variation in steel tested at 600 °C

4. Measurement of CTOA Curve for Aluminum 2014-T6

a) Room Temperature-Center Crack

The aluminum specimens were cut with a center crack in the **LT** direction using a water-jet machine. The specimens were of dimensions; length 2L=350mm, width W=88mm, thickness B=3.18mm. The crack size after the water jet cut was 2a_o=23mm. The notch of the crack after the water jet cut was sharpened on either side of the center-crack. The dimension of the crack after jewelers saw cut was close to 2a_o=25mm. All the specimens were fatigued at the rate of 8 Hz using a fatigue load of 0.5-15.5 kN. Specimens with two different fatigue crack lengths were tested. The fatigue crack obtained for the first specimen was of length 0.6mm and for the second specimen of length 5.5 mm.

The fatigue-cracked specimens were loaded under position control at the rate of 0.001 mm/sec. As the crack began to grow the loading was held constant at certain length of crack extension and the digital image captured. The captured digital images were used to obtain the CTOA with crack extension using MATLAB for the specimens tested. The stable crack extension for both the specimens was found to be less than 4 mm. Figure 11 shows images captured at very small crack extensions. The specimens failed after a small stable crack extension. Figure 12 shows a picture of the fractured center cracked aluminum specimen tested in Mode I loading. Figure 13 shows the fractured surface.
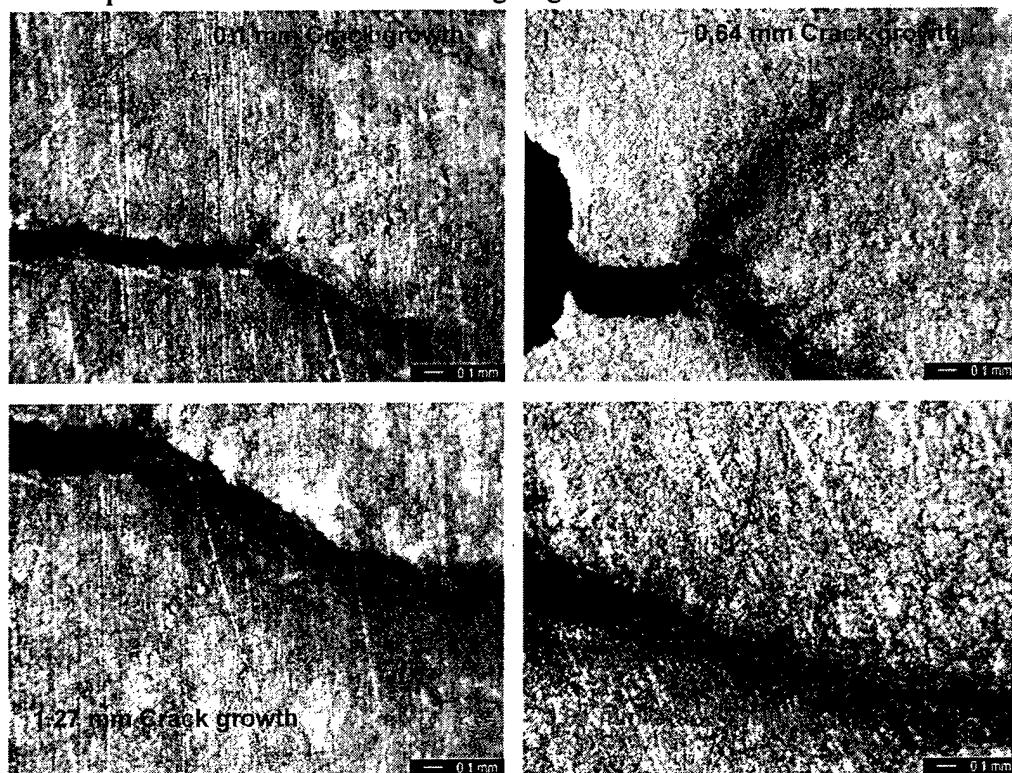
Fig. 11 Crack tip region at various stages of crack growth for aluminum specimens tested at room temperature mperature
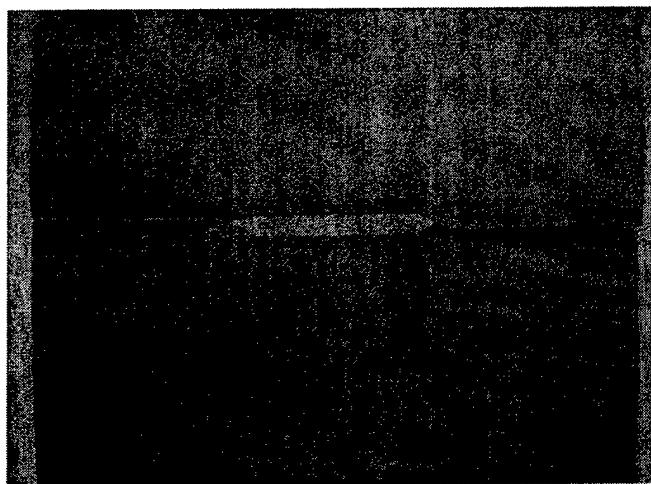
Fig. 12 Fractured center crack specimen tested in Mode I loading
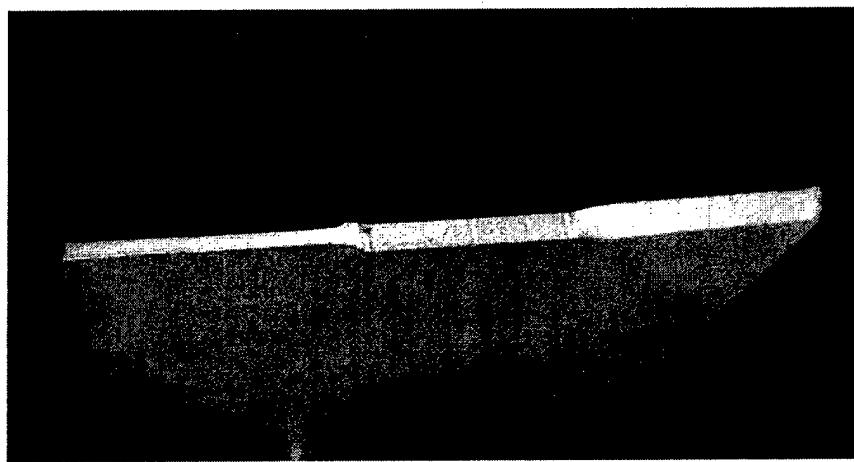
Fig. 13 Fractured surface of the center crack specimen tested in Mode I loading

b) Room Temperature-Edge Crack

The tests with center crack specimens gave very few data points for the CTOA resistance curve for Aluminum Al-2014-T6 since the length of stable crack propagation was about 4mm. To get more data and also to check the effect of crack geometry and dimensions on the CTOA resistance curve, edge crack specimens with two different widths were used. The specimens were cut with edge crack using a water-jet machine. Following the water jet cut the notch was sharpened with a jewelers saw and fatigue loading was applied to produce a sharp crack. The specimens are of dimensions as shown in Table 1. All the specimens were fatigued at the rate of 8 *Hz* using the fatigue load range shown in Table 1.

Table 1 Final dimensions of edge cracked specimens after fatigue loading

Specimen	W (mm)	2L (mm)	Thickness t (mm)	Fatigue Load (kN)	No. of cycles	Final Crack Size, 2a₀ (mm)
EC1	150	328	3.2	0.5-20.5	1923	48.50
EC2	75	354	3.2	0.5-10.5	4527	29.40
EC2	75	354	3.2	0.5-10.5	5010	29.52
EC2	75	354	3.2	0.5-10.5	5000	28.44

The fatigue-cracked specimens were loaded under stroke control at the rate of 0.001 *mm/sec*. As the crack began to grow the loading was held constant at certain length of crack extension and the digital image captured. The captured digital images were used to obtain the CTOA with crack extension using MATLAB for the specimens tested. The stable crack extension for the edge crack specimen with the large width was close to about 12.7 mm. For the edge crack specimen with a smaller width (75 mm) there was a similar length of stable crack extension of about 15mm. For this reason three edge crack specimens with the smaller width were tested to obtain more CTOA data. The data obtained from the CTOA measurement using the acquired digital images from the fracture tests are shown in Fig. 14 which also includes the data from center cracked specimens. Figure 15 shows images captured at different crack extension lengths using the edge crack specimen. Fig.16a shows the larger width edge crack specimen EC1 and Fig. 16b shows the edge crack specimen with the smaller width. Specimens of type EC1 are too wide to be placed directly into the hydraulic grips of the load-frame. Hence these specimens were bolted to a fixture which was gripped by the hydraulic grips.
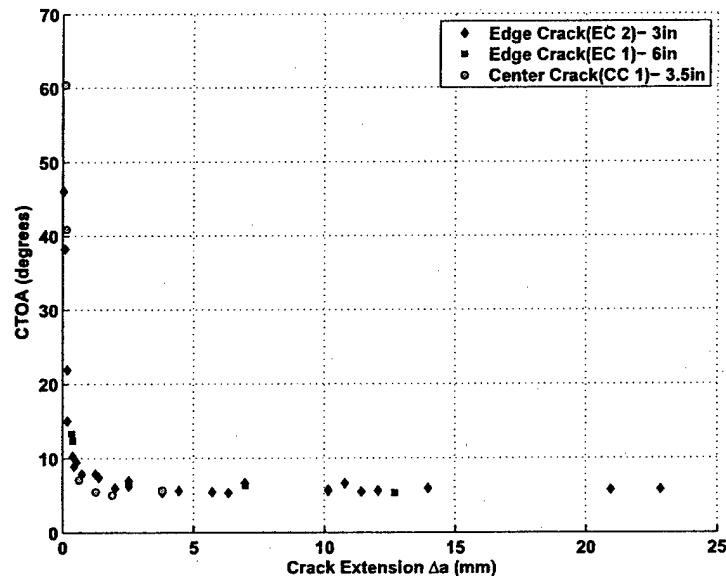
Fig. 14 CTOA resistance curve for Aluminum 2014-T6
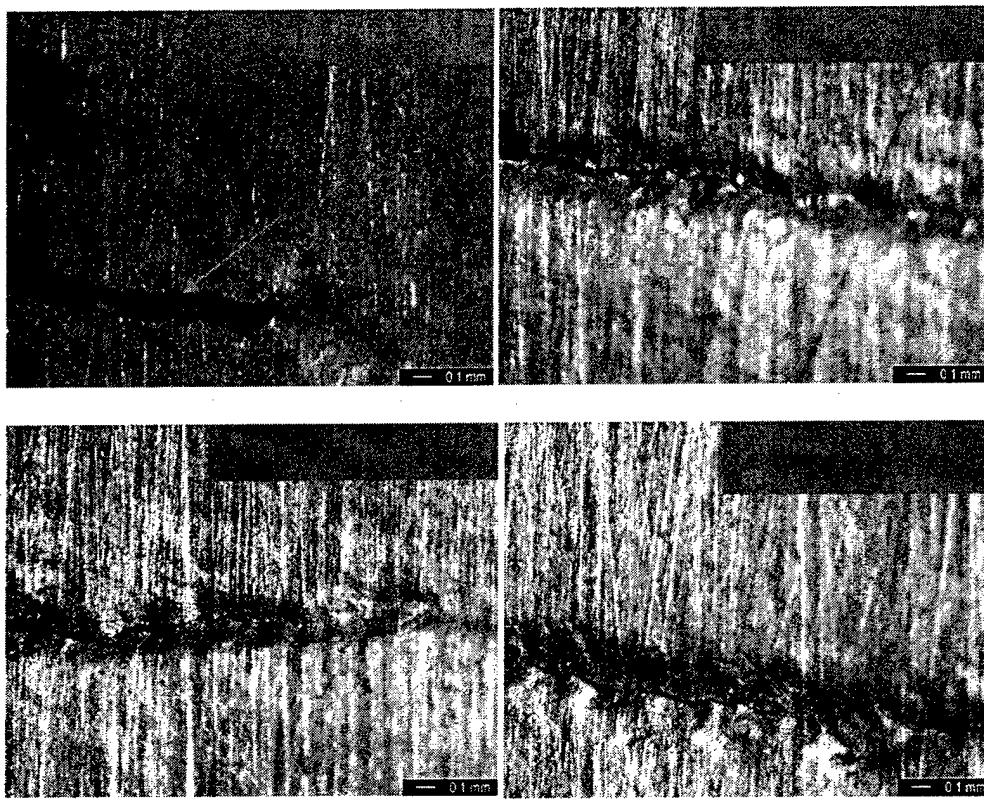
Fig. 15 Crack tip region at various stages of crack growth for edge crack specimens EC2
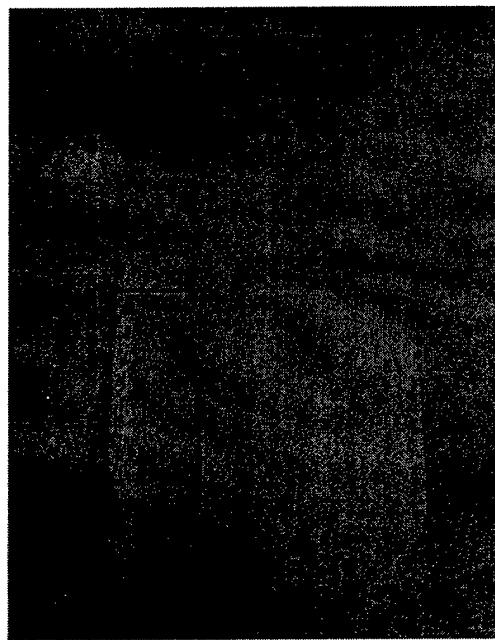
Fig. 16a Edge cracked specimen EC1 with width W=150 mm
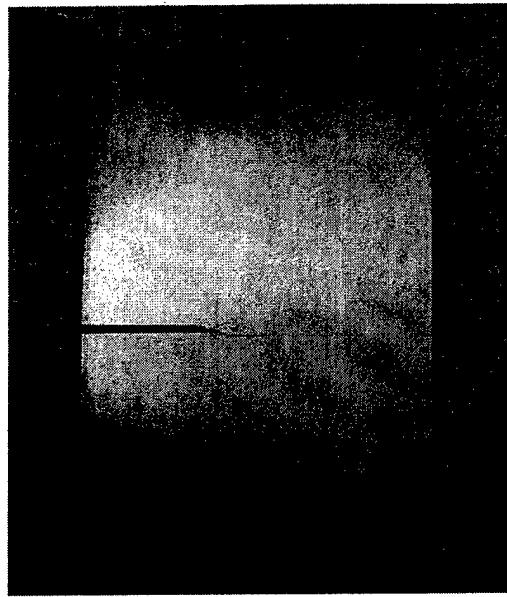
Fig. 16b Edge cracked specimen EC2 with width W=75 mm

c) Al 2014-T6 Tested at 100°C and 200°C

The measurement of CTOA in Al 2014 under 100°C and 200°C was conducted in a way similar to that for duplex steel. The data are presented in Fig. 17.
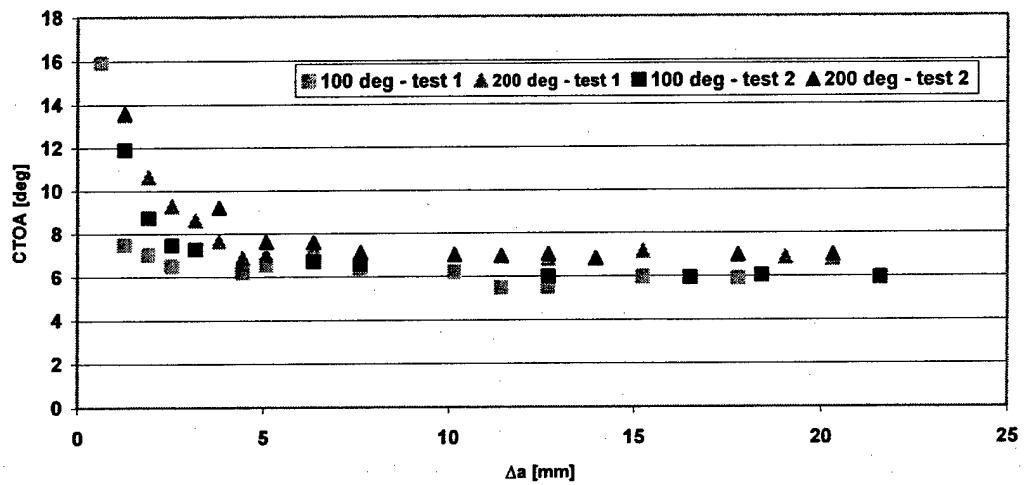
Fig. 17 CTOA data for Al 2014-T6 at 100°C and 200°C.

Part II Simulation of Burst of Thin-Walled Cylinders

1. Duplex Steel

1.1 CTOA Curves

a) Room Temperature CTOA curve:

The room temperature CTOA curve was obtained in the previous phase of the project. The CTOA curve obtained from fitting test data was obtained as

CTOA =-0.003(Δa)^3+0.162(Δa)^2-2.967(Δa) +28.179 for Δa <15mm;
CTOA = 10° for Δa > 15mm.

The CTOA curve is shown in Fig. 1.
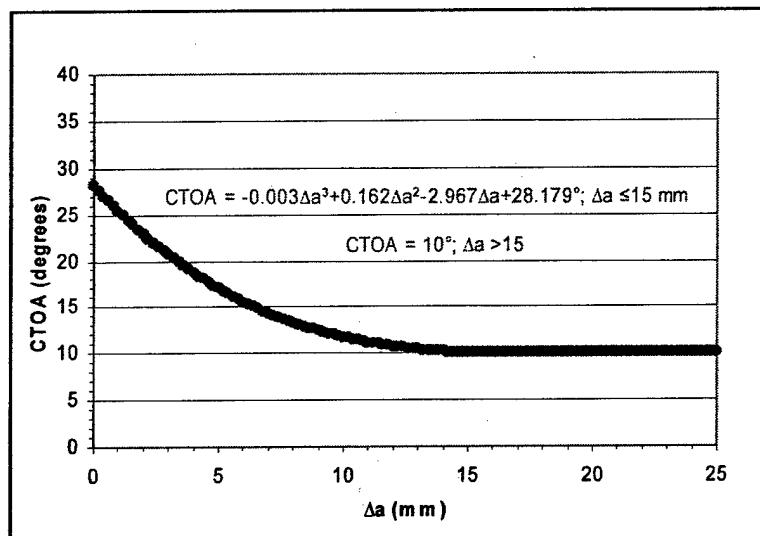
Fig. 1 CTOA curve for duplex steel at room temperature

b) CTOA curves at Elevated Temperatures

CTOA vs crack extension data at elevated temperatures have been experimentally obtained as described in Part I of this report. The data are fitted into polynomial functions as follows.

• **200 degree CTOA curve:**

CTOA = -0.0085(Δa)^3 + 0.3726(Δa)^2 - 5.2002(Δa) + 29.969° for Δa $\leq$ 11.5mm;
CTOA = 6.5156° for Δa > 11.5mm.

- **400 degree CTOA curve:**

$CTOA = -0.0179(\Delta a)^3 + 0.5716(\Delta a)^2 - 5.7576(\Delta a) + 28.594°$ for $\Delta a \leq 8.9mm$;
$CTOA = 10°$ for $\Delta a > 8.9mm$.

- **600 degree CTOA curve:**

$CTOA = -0.0123(\Delta a)^3 + 0.3701(\Delta a)^2 - 3.4023(\Delta a) + 33.541°$ for $\Delta a \leq 7.1mm$;
$CTOA = 23.6391°$ for $\Delta a > 7.1mm$

Figures 2-4 show the fitted CTOA curves for the three elevated temperatures, respectively. For comparison, all curves are presented in Fig. 5.
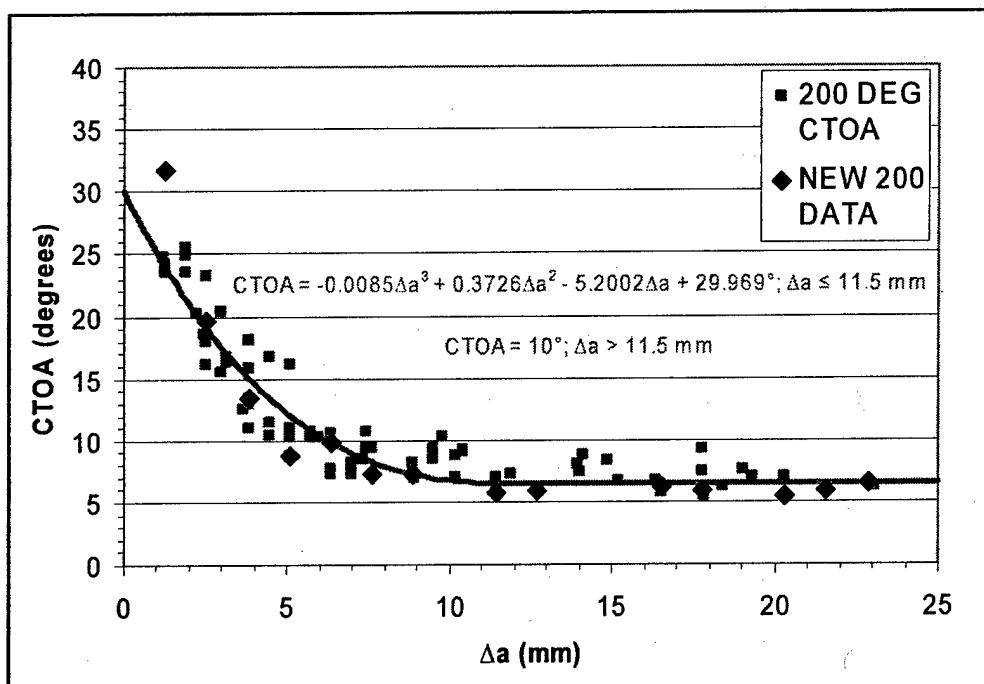
Fig. 2 CTOA curve for duplex steel at 200°C
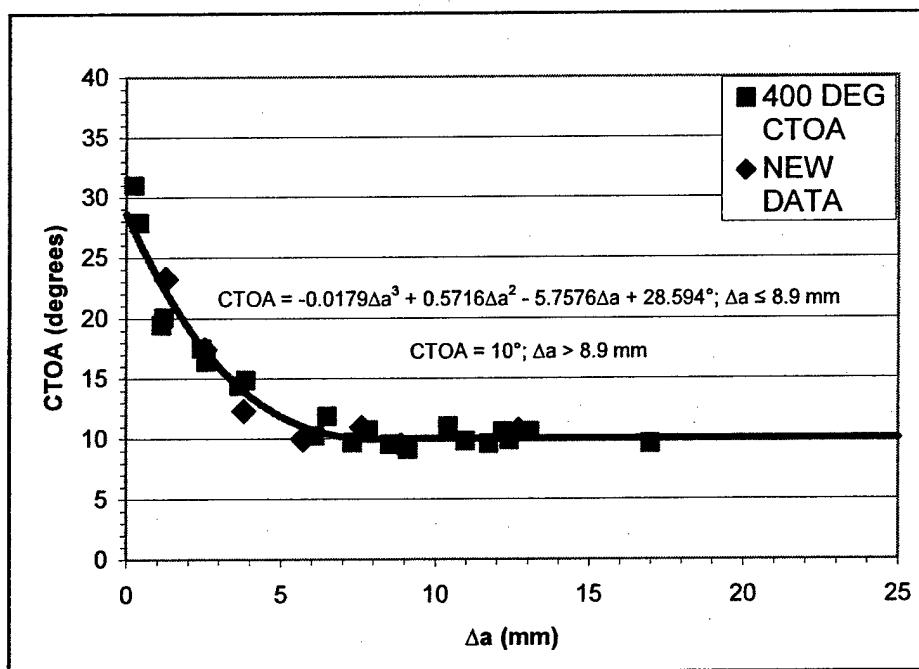
Fig. 3 CTOA curve for duplex steel at 400°C

$CTOA = -0.0179\Delta a^3 + 0.5716\Delta a^2 - 5.7576\Delta a + 28.594°; \Delta a \leq 8.9$ mm

$CTOA = 10°; \Delta a > 8.9$ mm
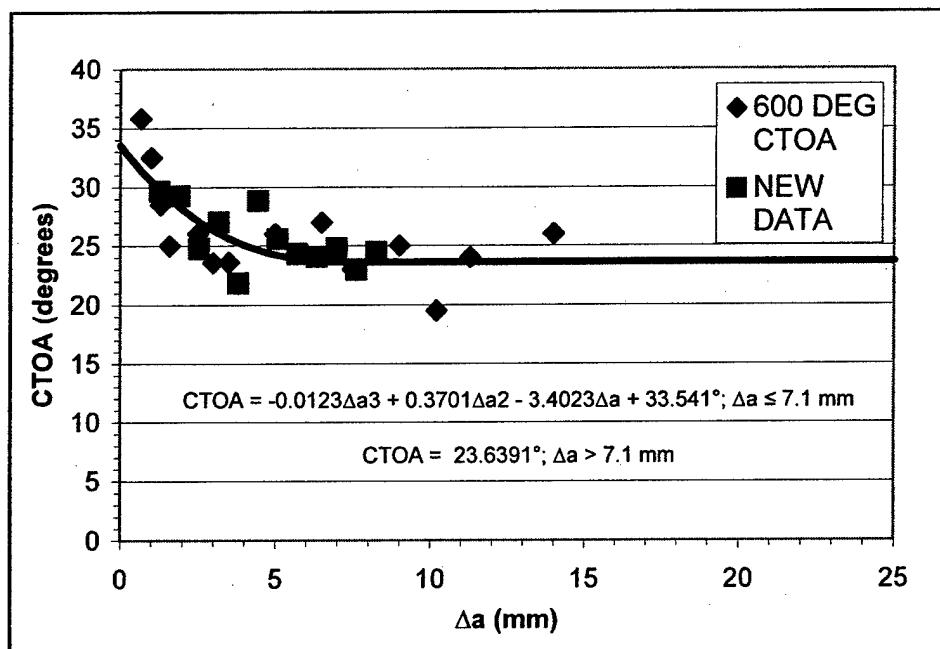
Fig. 4 CTOA curve for duplex steel at 600°C

$CTOA = -0.0123\Delta a3 + 0.3701\Delta a2 - 3.4023\Delta a + 33.541°; \Delta a \leq 7.1$ mm

$CTOA = 23.6391°; \Delta a > 7.1$ mm
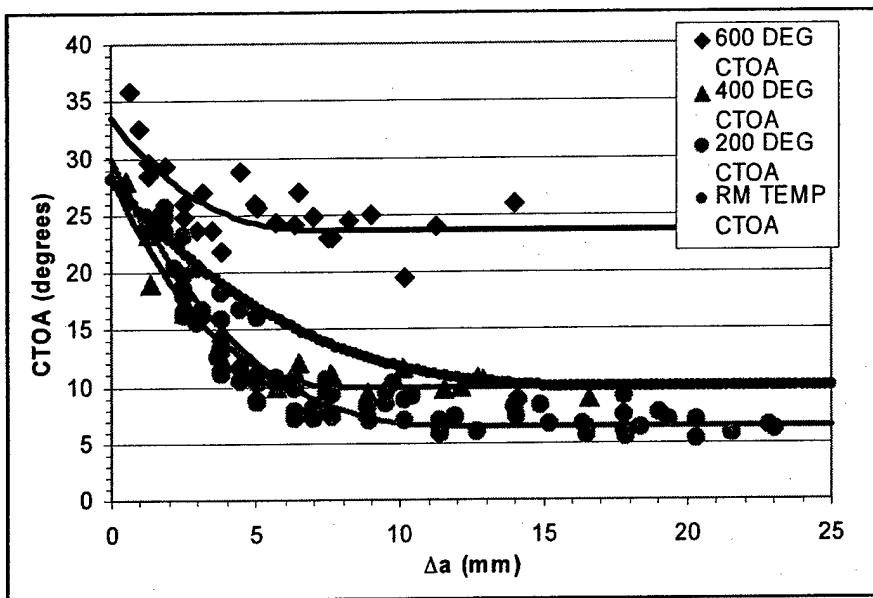
Fig. 5 Comparison of CTOA curves of duplex steel for various temperatures

1.2 Temperature-dependent Mechanical Properties

Besides the CTOA curves, we also need the mechanical properties of duplex steel in the temperature range of interest. From Fig. 6 which shows the Young's modulus of duplex steel as a function of temperature, we note that Young's modulus of duplex steel is nearly linear with respect to temperature. Hence, we adopted this approximation for Young's modulus in the temperature range of interest.
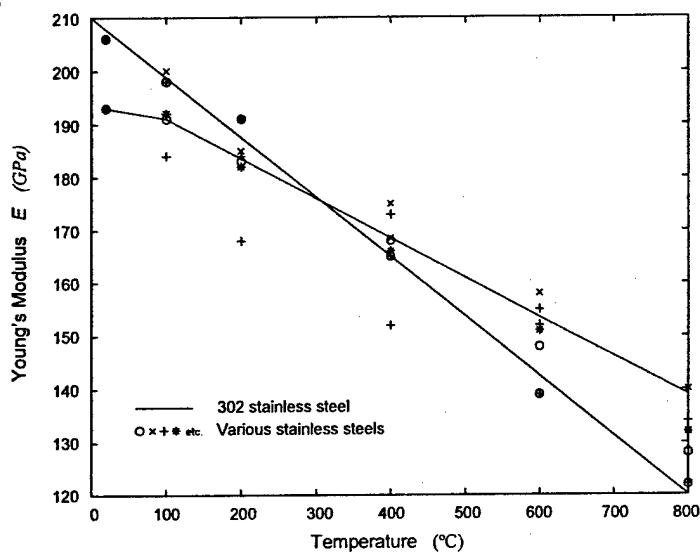
Fig. 6 Young's modulus of duplex steel vs temperature

20

The yield stress as a function of temperature was found by multiplying the room temperature yield stress by a certain percentage as plotted in the Military Handbook of Materials 5 for duplex steels including 301, 302, and 304. Figure 7 is a reproduction showing this relationship. It is specifically for alloy 301 but stated its usefulness for the other duplex steels so this was used to obtain the yield stresses for the high temperature stress strain curves and also the plastic portion of the curve as shown in Fig.8. A curve fit of the data was done to estimate the yield strength at the desired temperatures more accurately. The stress strain data for room temperature was that obtained by previous experiment done in the lab. These stress strain plots were then transferred as temperature dependant material data into the ABAQUS input file.

The coefficient of thermal expansion was treated in a similar manner. Having data points for 20°C and 1000°C a straight line approximation was assumed to obtain the coefficient of thermal expansion specific for 200°, 400°, 600°, and 800°C. The values used in the analysis are listed in following table.

Temperature (°C)	α_T
20	$12*10^{-6}$
200	$13.477*10^{-6}$
400	$15.117*10^{-6}$
600	$16.757*10^{-6}$
800	$18.397*10^{-6}$
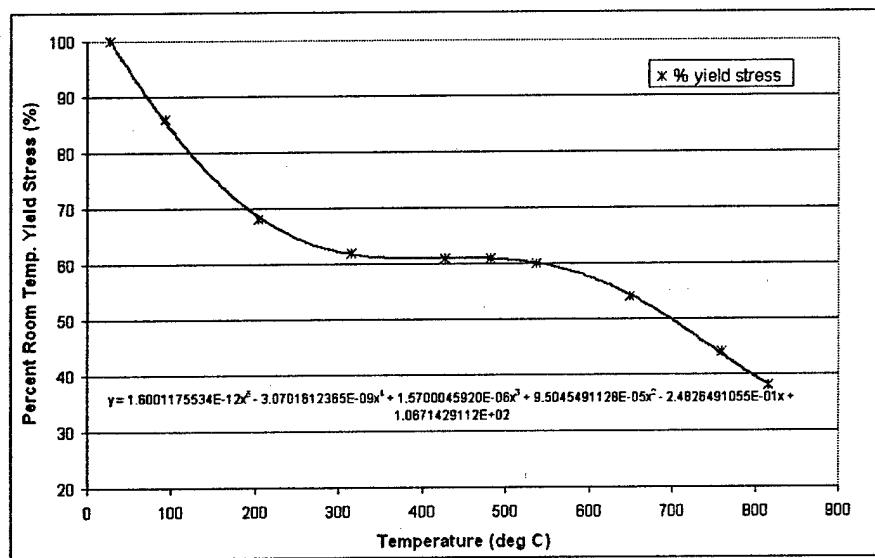
Fig. 7 Yield stress of duplex steels vs temperature
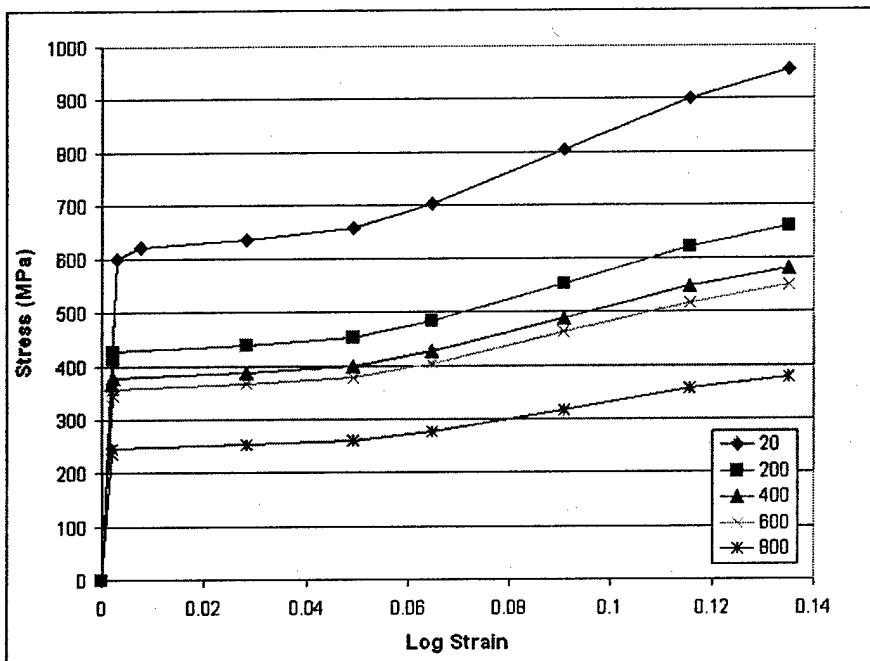
Figure 8 Constructed stress-strain curves for duplex steel

1.3 Simulation of Burst of Steel Cylinders

a) Geometry and finite element model

The steel cylinder to be analyzed is 25.4 cm (10 in.) in diameter and has a 1.5mm wall thickness. Four crack lengths, 3, 6, 9, and 12 cm, are considered. The elevated temperature region is assumed to be circular in shape with a transition zone from high temperature (800°C) to room temperature of 1.02 cm. This transition zone is broken into three equidistant regions of 0.34 cm each as shown in Fig. 9. In Fig. 9, six of the rings can be seen and the crack tip is located along the edge between the 3rd and 4th ring. This configuration allows up to four different configurable positions for the high temperature region in order to investigate how the burst pressure behaves with respect to different initial crack tip positions. Four cases of temperature and crack tip positions are considered as follows.

Case 1: Room temperature cylinder
Case 2: High temperature applied with the crack tip stopping at room temperature.
Case 3: High Temperature applied with the crack tip stopping at 200 °C.
Case 4: High Temperature applied with the crack tip stopping at 400 °C.

22
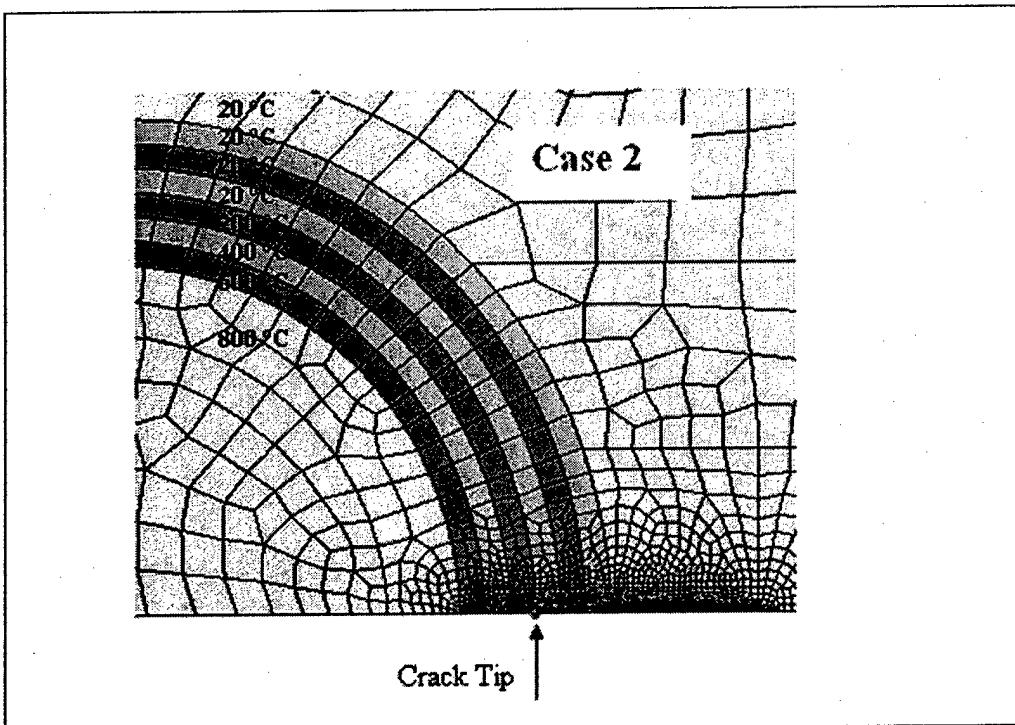
Fig. 9 Temperature zones of the finite element cylinder model.

b) Analysis Method

The first step in the simulation analysis is to apply thermal loading to the cylinder. The temperature load is applied first in a two step ABAQUS input file so that a steady state temperature can be assumed for the remainder of the test. The model is then brought from room temperature (20 °C) to the various field temperatures of 20, 200, 400, and 600 °C. Once the temperature loading has been made, step 2 of the analysis places the cylinder into its first increment of pressure loading. Once the pressure is applied ABAQUS exits and the post processor takes control. First the needed data sets are obtained from the ABAQUS *.fil file with the program *makedata* then these are sent into the computational program *newctoa.out* to be scrutinized. Upon entry into *newctoa.out* the crack tip opening angle (CTOA) is calculated by averaging the node displacement angles for the nodes along the crack face just in front of the crack tip between 0.2 to 1.0 mm. The average of their angles makes up what is called the CTOA.

The next step is to use the crack tip location to determine its temperature and also the crack tip extension value (Δa) to be fed to the critical angle calculation so the correct CTOA curve can be used to calculate the critical angle. For room temperature, Δa would remain constant, but since there is a different CTOA curve for each transition temperature, the program switches between curves. The ideal way to do this is to transition horizontally to the new CTOA curve at the same angle previously obtained on the old curve. This setback/forward value is predetermined using the constant transition

23

locations of the temperature fields and the temperature specific CTOA curves to calculate, first the angle (at 3.4 mm, for example), then the value of Δa at that angle on the new curve. The difference of the two Δa increments is the setback. These setback values are then set as constants in the program and are added to Δa throughout the remainder of the analysis, allowing the new CTOA curve to be followed until the next transition. This works well between areas of the curve where there is a place to step to. But in the case of the 200 °C curve, it drops below the room temperature constant of 10° by the time the transition is to take place, if case 4 is being run for example. In this case the current Δa plus setback are retained and a vertical jump is allowed and that angle on the room temperature CTOA curve is used.

This is all done to calculate the driver of the analysis which is the critical angle. The critical angle is determined from the temperature specific CTOA curves at each point in the analysis to compare to the CTOA results obtained from ABAQUS. For fracture to occur the CTOA must equal the critical angle within the tolerance of 0.07 degrees or else the input load is modified and the analysis is run again for the same crack tip. If the angle is too large, the load is decreased and vise versa if the angle is to small the load is increased.

Once the correct angle is reached, the boundary condition on that node is released and the next node is analyzed. Every time a node is released the data is then stored in an output file named *ctoa_hist.dat*.

The program *newctoa.out* acts as both post processor and preprocessor in its duties. It does the portion of the analysis described above and it also prepares the new input file to be fed into ABAQUS for all subsequent steps. Once it is finished, one other little program checks the results to see whether the cylinder was previously overloaded or not before proceeding to the next step. This program is named *resdec.out* and if the structure was overloaded, *resdec.out* causes ABAQUS to use the new input file with a previously non overloaded restart file to avoid the improper plasticity history of being overloaded.

Once the peak pressure is found, the program is run out or allowed to end prematurely due to instability of the problem after this point. It is assumed that fracture occurs at the peak pressure so furthering the test is not necessary except in case 4 where the jump up to the room temperature CTOA curve means a pressure increase even after an initial peak is reached. This is performed to determine if the first or second peak pressure is the highest.

c) Simulation Results

The simulation results are presented in Tables 1- 4 for the four cases of crack length, respectively. In these tables, the burst pressures (for room temperature) obtained in the previous phase of the project are also included for comparison. The present simulation is seen to yield slightly higher burst pressures which are closer to the test data. Since the analysis procedures are basically the same, the only possible explanation of this small difference could be due to fact that the finite element meshes used in the present simulation is finer than that used in the previous work.

Table 1 High temperature burst pressure of a steel cylinder with 12 cm crack

Crack Length 2a	Thickness t (mm)	Assumed Temperature at Initiation Crack Tip	P_{MAX} (MPa)	(%) Different from P_{max} @ Rm Tmp	Crack Growth at Peak Press (mm)	P_{INIT} (MPa)
12cm	1.5	400	1.89	2.1 (1.6)	6.8	0.96
12cm	1.5	200	1.92	0.5 (3.2)	4.6	1.06
12cm	1.5	20	1.91	1.0 (2.7)	5.8	1.04
12cm	1.5	RM TEMP	1.93 (1.86)	3.8	6.2	1.04

*Values in parentheses at room temperature are from previous simulation

Table 2 High temperature burst pressure of a steel cylinder with 9 cm crack

Crack Length 2a	Thickness t (mm)	Assumed Temperature at Initiation Crack Tip	P_{MAX} (MPa)	(%) Different from P_{max} @ Rm Tmp	Crack Growth at Peak Press (mm)	P_{INIT} (MPa)
9cm	1.5	400	2.45	(2.7)	6.8	1.44
9cm	1.5	200	2.52	(0.0)	4.0	1.53
9cm	1.5	20	2.50	(0.8)	4.6	1.53
9cm	1.5	RM TEMP	-- (2.52)	--	4.6	1.53

Table 3 High temperature burst pressure of a steel cylinder with 6 cm crack

Crack Length 2a	Thickness t (mm)	Assumed Temperature at Initiation Crack Tip	P_{MAX} (MPa)	(%) Different from P_{max} @ Rm Tmp	Crack Growth at Peak Press (mm)	P_{INIT} (MPa)
6cm	1.5	400	3.41	0.9 (2.4)	5	2.25
6cm	1.5	200	3.53	2.6 (6.0)	3.6	2.39
6cm	1.5	20	3.48	1.2 (4.5)	3.6	2.41
6cm	1.5	RM TEMP	3.44 (3.33)	3.3	3.4	2.27

Table 4 High temperature burst pressure of a steel cylinder with 3 cm crack

Crack Length 2a	Thickness t (mm)	Assumed Temperature at Initiation Crack Tip	P_{MAX} (MPa)	(%) Different from P_{max} @ Rm Tmp	Crack Growth at Peak Press (mm)	P_{INIT} (MPa)
3cm	1.5	400	5.24	5.3 (3.1)	3.6	4.16
3cm	1.5	200	5.50	0.3 (1.9)	2.6	4.45
3cm	1.5	20	5.52	0.0 (2.2)	2	4.60
3cm	1.5	RM TEMP	5.52 (5.40)	2.2	2 (1.8)	4.51

From the simulation result presented in Tables 1-4, it is interesting to note that the burst pressure of the cylinder for a given crack length does not seem to be affected significantly by the presence of the high temperature zone. There is only a slight indication that the burst pressure decreases with increased temperature application.

Figures 10 – 13 show the pressure-crack extension curves of the four crack lengths for different temperature conditions. Figure 14 presents a comparison of the pressure vs. crack-extension curves for the four crack lengths under case 4 load conditions.
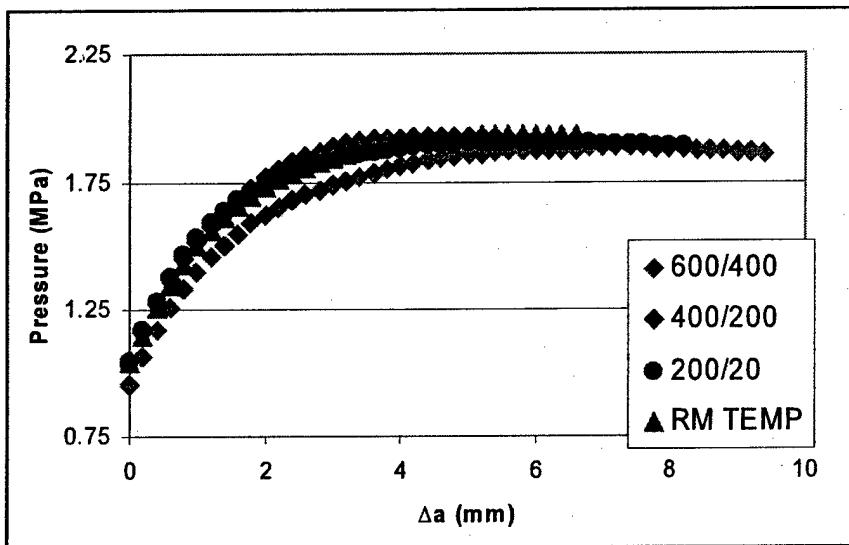
Figure 10 Internal pressure vs. crack extension plot for 12cm crack length
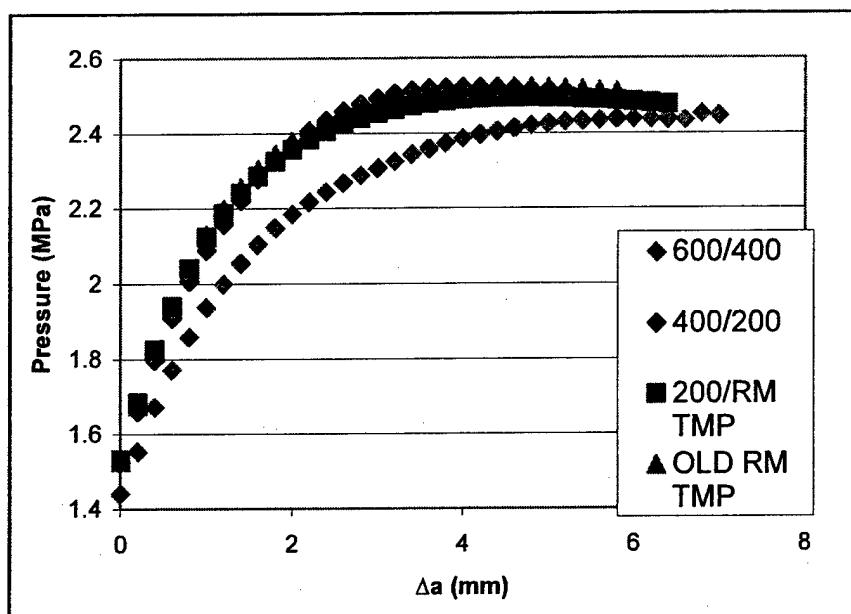
Figure 11 Internal pressure vs. crack extension plot for 9cm crack length

Figure 12 Internal pressure vs. crack extension plot for 6cm crack length
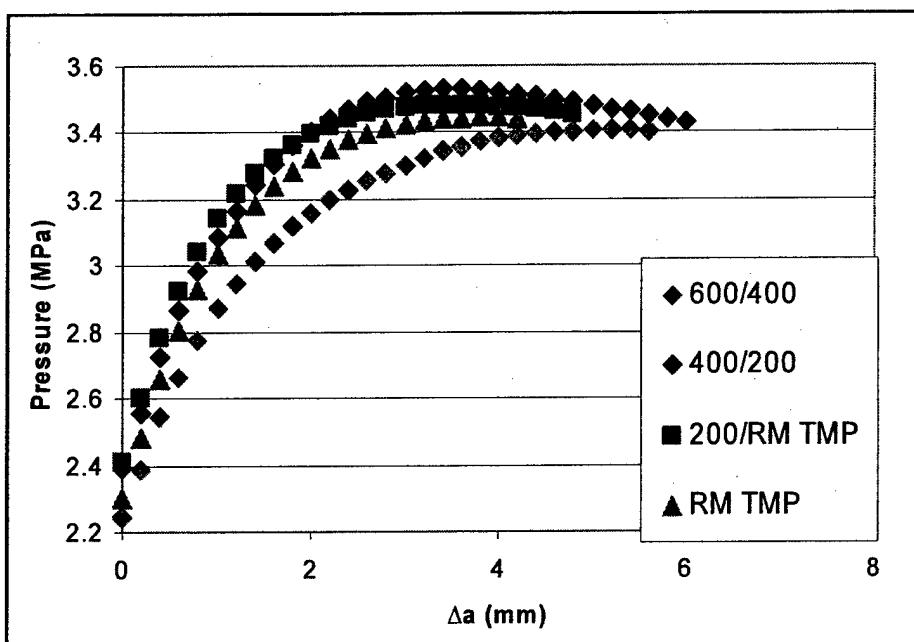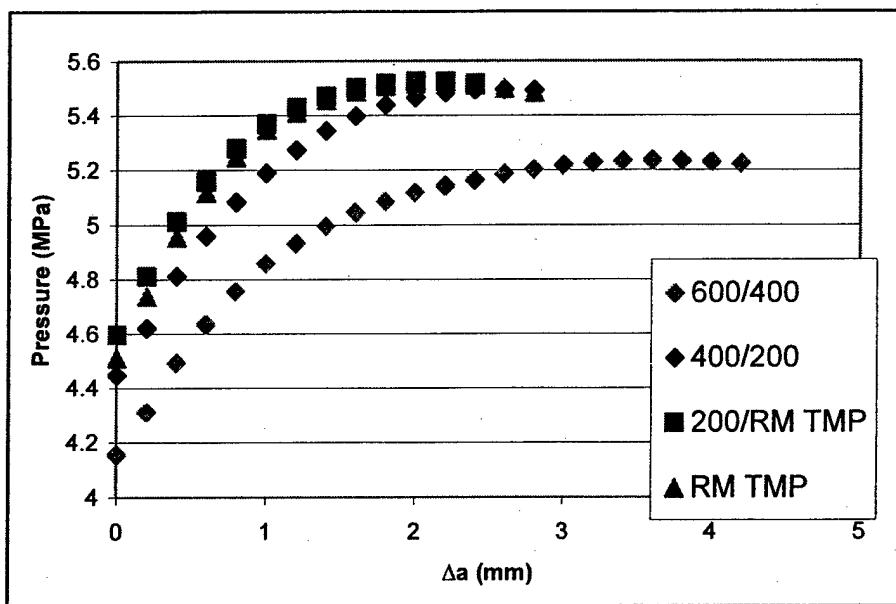
Figure 13 Internal pressure vs. crack extension plot for 3cm crack length
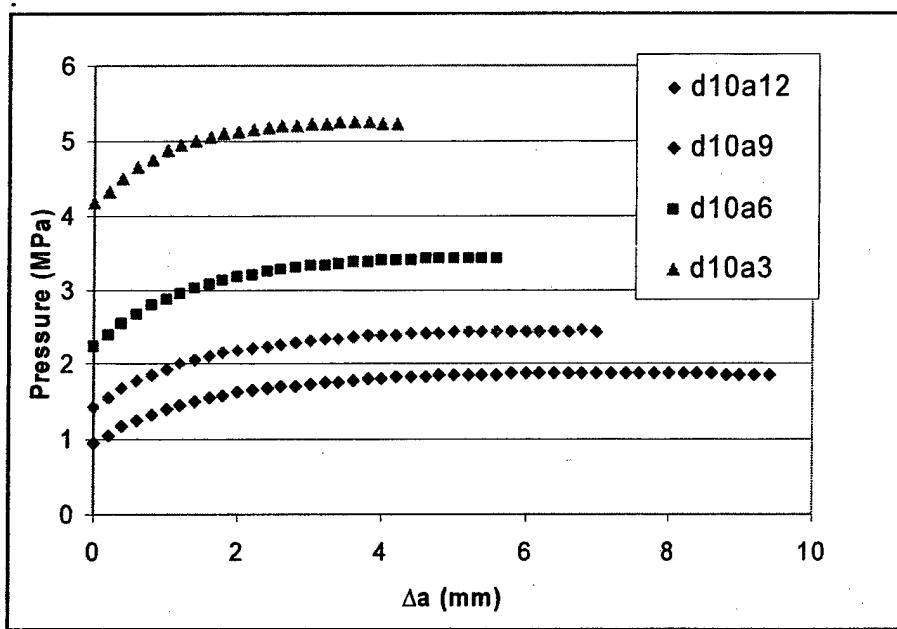
Figure 14 Comparison of case 4 pressure vs. crack extension curves for different crack lengths

2. Aluminum 2014-T6

2.1 CTOA Curve

a) Room Temperature CTOA Curve

The CTOA data presented in Fig. 15 for Aluminum 2014-T6 at room temperature are used for the polynomial fit. The result is given as

$$CTOA = -0.2471(\Delta a)^3 + 2.601(\Delta a)^2 - 8.3(\Delta a) + 14.1, \quad 0 \le \Delta a \le 2.45\,mm$$

$$CTOA = 5.74, \quad \Delta a > 2.45\,mm$$

Figure 15 shows the CTOA curve and the data.
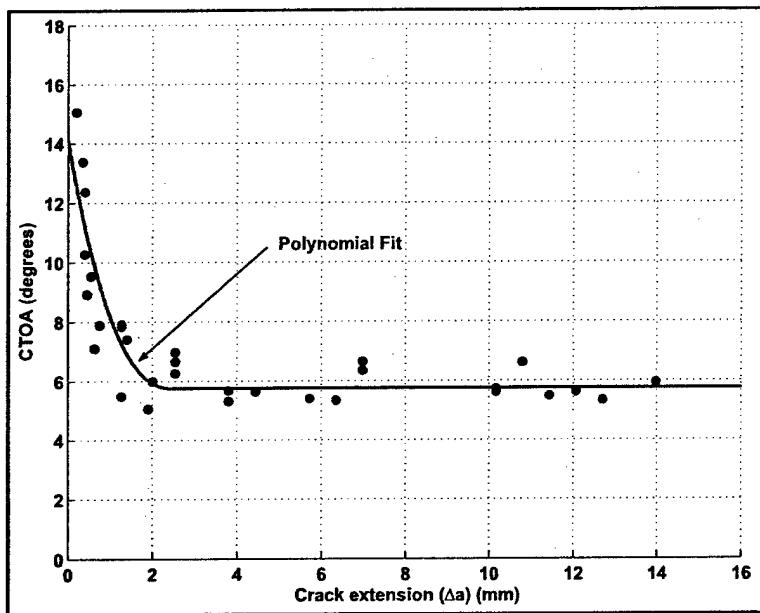
Fig. 15 Polynomial fit of the CTOA data for Aluminum 2014-T6 at room temperature

b) CTOA Curve for 100°C

The CTOA curve for 100°C is described by the following.

$$CTOA = -0.0081\Delta a^3 + 0.702\Delta a^2 - 5.1322\Delta a + 15.75°; \quad 0 \le \Delta a \le 4\,mm$$
$$CTOA = 5.9348°; \quad \Delta a > 4\,mm$$

The polynomial fit is shown in Fig. 16.

29

c) CTOA Curve for 200°C

The CTOA curve for 200°C is described by the following.

$CTOA = -0.0231\Delta a^3 + 0.5845\Delta a^2 - 4.5253\Delta a + 17.95°$; $0 \leq \Delta a \leq 6$ *mm*

$CTOA = 6.8506°$; $\Delta a > 6$ *mm*

The polynomial fit is shown in Fig. 16 along with 100°C.
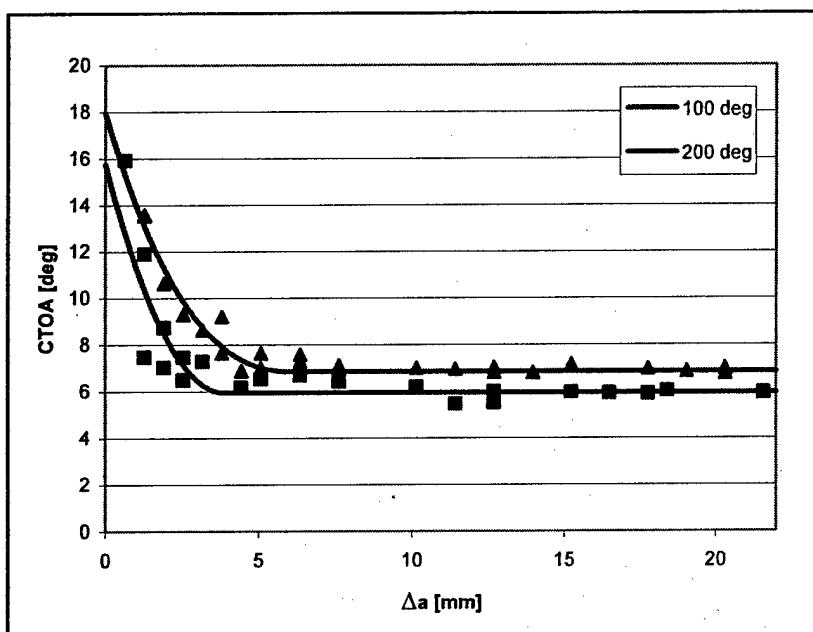
Fig. 16 Polynomial fit of the CTOA data for Aluminum 2014-T6 at 100°C, and 200°C.

2. 2 Material Properties for Al-2014-T6

The stress-strain curve was obtained from tests conducted on dog-bone specimens. Strain gauges were used to measure strains in the range from 0 to 5%. The large strains occurring during the test were determined using the laser extensometer. The strains measured using the laser were obtained from 0 to 16% strain. However the measurements from strain gauge are more accurate than the laser for small strains. Figure 17 shows the stress-strain data for strain up to 5%. The Young's modulus for the material is found to be around 70 GPa. The material has a yield stress of about 425 MPa. Figure 18 shows the complete stress-strain curve obtained. For the elastic-plastic modeling in ABAQUS eight points along the stress-strain curve in the range from 425 MPa to 517 MPa corresponding to the plastic strains ranging from 0% to 12.5% were used.
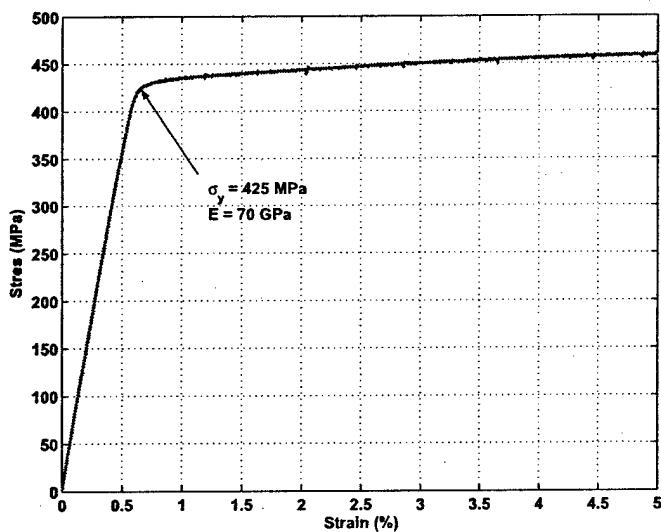
Fig. 17 Stress-strain curve for Al-2014-T6 at room temperature
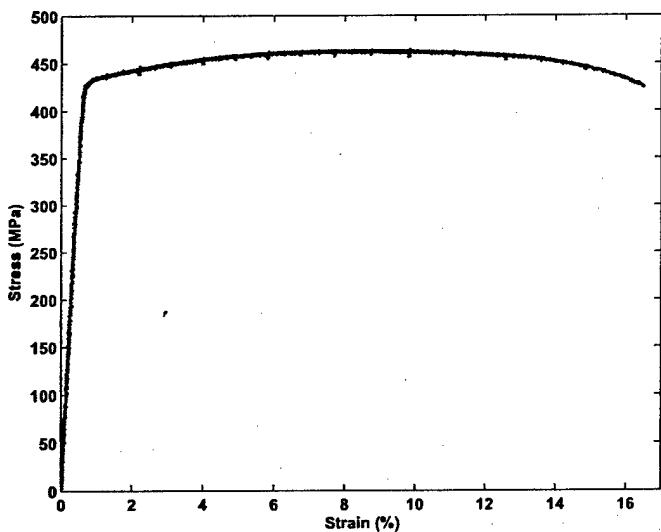
Fig. 18 Full range of stress-strain curve for Al-2014-T6 at room temperature

2.3 Temperature-dependent Mechanical Properties

Besides the CTOA curves, we also need the mechanical properties of Aluminum 2014-T6 in the temperature range of interest. From Fig. 19 which shows the Young's modulus of Aluminum 2014-T6 as a function of temperature, we note that Young's modulus drops more quickly as temperature increases. Hence, we adopted this approximation which was taken from Mil-Handbook-5 for Young's modulus in the temperature range of interest for

Aluminum 2014-T6 and is calculated by multiplying the room temperature value of Young's Modulus by the percentage indicated in the graph.
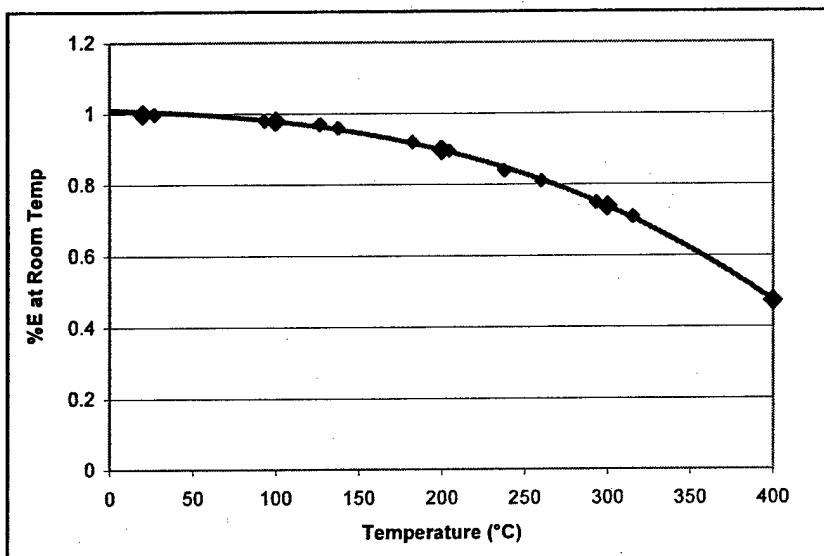
Fig. 19 Young's modulus of 2014-T6 Aluminum for elevated temperature (Mil-Hndbk-5)

The yield stress as a function of temperature was found in the same manner as Young's modulus by multiplying the room temperature yield stress by a certain percentage as plotted in the Military Handbook of Materials 5 for Al 2014-T6. Figure 20 is a reproduction showing this relationship as specified by Mil-Hndbk-5. It is specifically for Aluminum 2014-T6 so this was used to obtain the yield stresses for the high temperature stress strain curves and also the plastic portion of the curve as shown in Fig. 21. This estimation of yield stress was then compared with the test results at high temperature from our lab to validate the estimation. The stress strain data for room temperature was that obtained by previous experiment done in the lab, and for the case of 300°C the graphical estimate was lower then tested so the data gathered from the lab was used for the yield stress at that temperature in all of the finite element analyses. These stress strain plots were then transferred as temperature dependant material data into the ABAQUS input file.

The data for the coefficient of thermal expansion were treated in a similar manner as they were taken from Fig. 22 reproduced from Mil-Hndbk-5 for the coefficients of thermal expansion specific to 20°, 100°, 200°, 300 °, and 400°C and subsequently used for the Abaqus input file's material property definition. The values used in the finite element analysis are listed in the following table.

32

Aluminum 2014-T6 Material Properties for High Temperature			
T (°C)	E_{LT} (GPa)	σ^{YS} (MPa)	α (cm/cm-°C)
20	70	425.0	$22.29*10^{-6}$
100	68.536	403.8	$23.05*10^{-6}$
200	62.842	263.7	$23.81*10^{-6}$
300	51.693	111.5	$24.34*10^{-6}$
400	33.124	24.6	$24.65*10^{-6}$
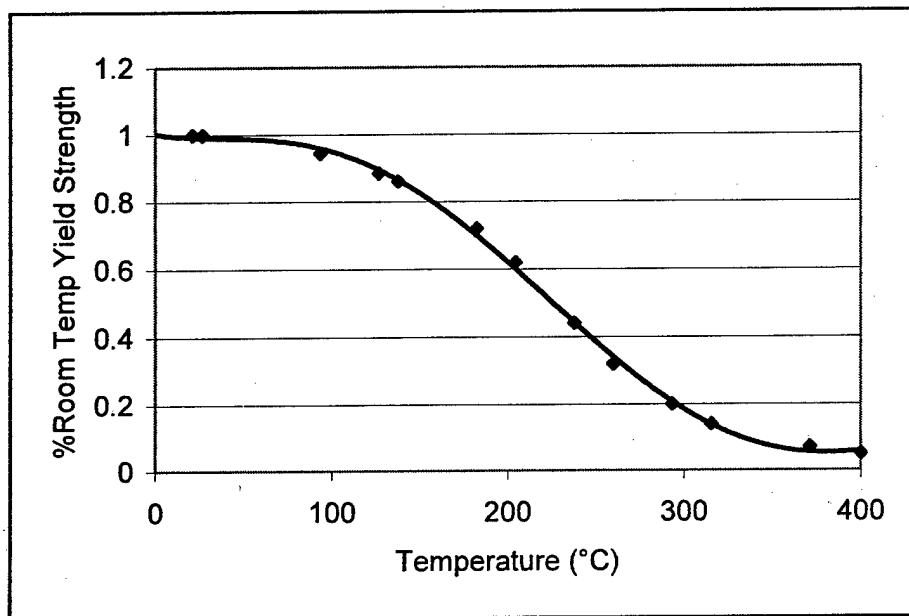
Fig. 20 Yield stress of Aluminum 2014_T6 vs. temperature (Mil-Hndbk-5)
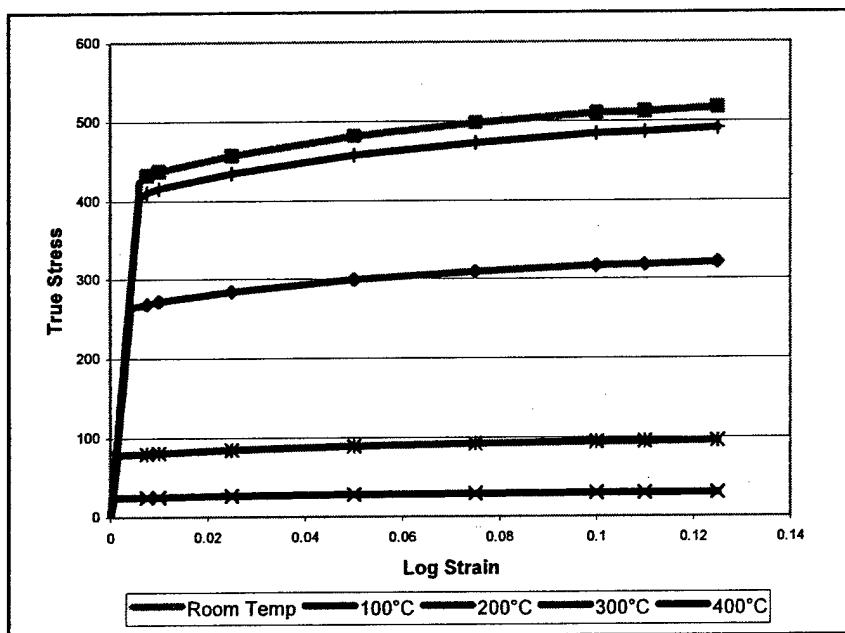
Figure 21 Constructed stress-strain curves for Aluminum 2014-T6
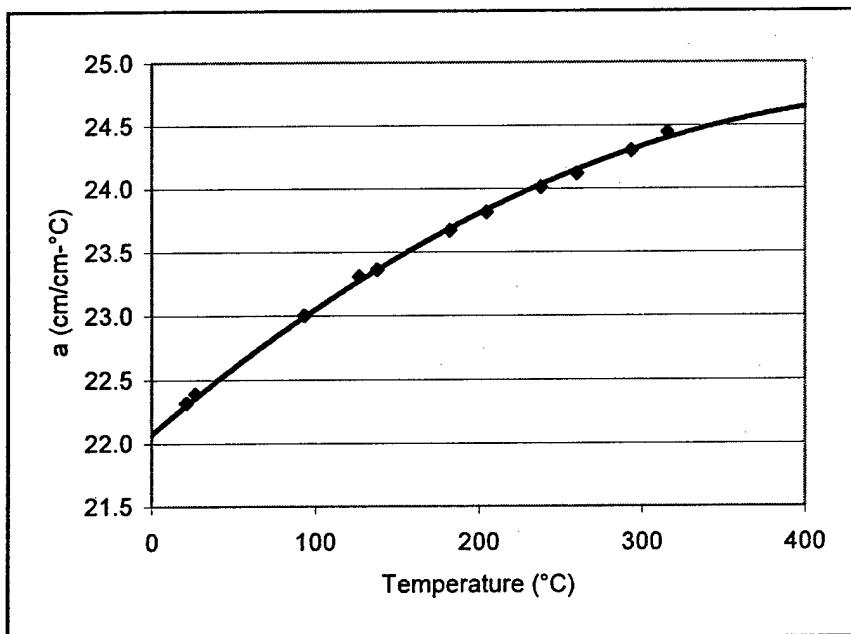
Figure 22 Coefficient of Thermal Expansion for Aluminum 2014-T6

2.4 Simulation of Burst of Aluminum Cylinders at Room Temperature

The dimensions of the closed cylinder are listed in Table 5. Using the double symmetry of the model and the loading condition one fourth of the model was used in the simulation. Four noded shell elements (S4) were used to mesh the model. Four different lengths of the initial crack, namely 2a = 4, 8, 10, 14 cm were considered while maintaining the diameter of the cylinder to be the same value of 25.4 cm (10 inches) for all the cases. The thickness of the cylinder was chosen to be the same as the Al-2014 material used for the fracture tests, namely 3.2mm. Figure 23 shows a representative mesh of the one-fourth model of the cylinder with the crack tip and the end cap indicated.

Table 5 Cylinder dimensions used in the study

Cylinder	Diameter (D) (mm)	Length (L) (mm)	Crack Length (2a) (mm)	Thickness (mm)
1	254 (10 in)	722	40	3.2
2	254 (10 in)	742	80	3.2
3	254 (10 in)	752	100	3.2
4	254 (10 in)	772	140	3.2
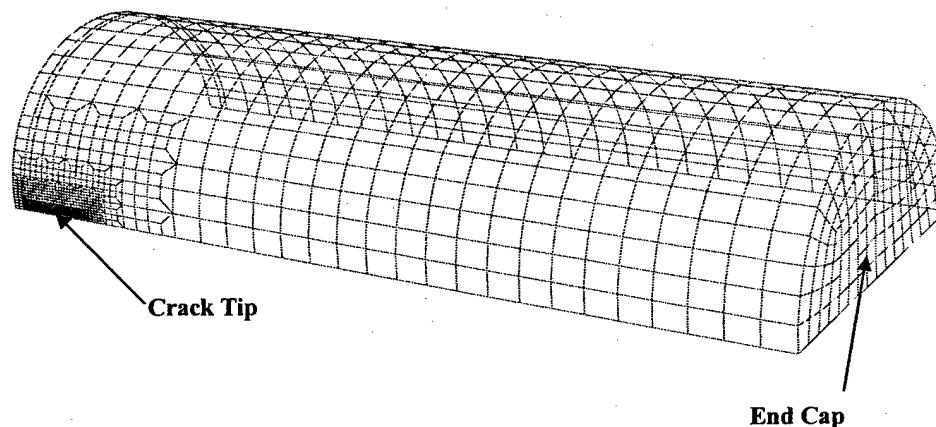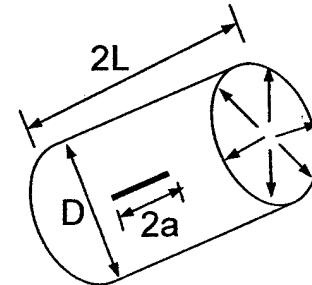
Fig. 23 The mesh used in the analysis

The critical CTOA criterion, which implicitly accounts for material non-linearity is used as the appropriate parameter for the modeling of the fracture of the cylinder. This section discusses the use of this parameter for the case of the cylinder shell subjected to internal pressure. As discussed in the previous section for steel, the CTOA criterion is applied to

Mode I fracture to determine the critical (or burst) pressure of the closed cylinder with internal pressure as the loading condition. The ABAQUS software is used to perform the finite element analysis (FEA) at every load step. Using the nodal displacements at every load step the opening angle is computed and compared with the critical CTOA using a C++ program. After the check of the opening angle the C++ program computes the load, the location of the crack tip, the changed boundary conditions and writes the input file to be used to run the next load increment step using the ABAQUS FEA software. The above set of steps has to be repeated for every load increment made. A UNIX program is used for performing the ABAQUS FEA, extraction of nodal displacement data after the FEA, and running the C++ program in sequence for every load increment. If the opening angle is found to be more than the critical CTOA the pressure load is incrementally decreased until the opening angle matches the critical CTOA.

The material was modeled as elastic-plastic and the internal pressure was increased in small increments. The polynomial fit developed for the Al-2014 material was used as the crack growth criterion. The internal pressure was increased for crack growth initially. After the critical (or burst) pressure is reached further crack extension at a steady state would be possible by reducing the internal pressure by small amounts after every increment of crack growth. Figure 24 shows the pressure P_{INIT} for crack growth to initiate, the maximum pressure P_{MAX} (or burst pressure) for the cylinder and the corresponding crack extension. Tables 6 and 7 summarize, respectively, the burst pressure predictions using the small and large deformation theories for the cylinders with the four different initial crack lengths. The burst pressure was also predicted using the large deformation theory for the cylinder with crack length 2a=10 cm and 2a=14 cm and the burst pressures were found to be smaller than the values predicted using small deformation. However the predictions obtained using the small deformation and large deformation theory were found to be close and within 3%. It is noted that the crack growth at the burst pressure in the aluminum cylinder is shorter than that in the corresponding duplex steel cylinder.

Table 6 Burst pressure predictions for Al-2014 cylinders with small deformation

Cylinder	Diameter (mm)	Crack Length 2a (mm)	Thick t (mm)	P_{MAX} (MPa)	Crack Growth at Pmax Δa (mm)	P_{INIT} (MPa)
1	254 (10 in)	40	3.2	4.59	3.0	3.599
2	254 (10 in)	80	3.2	2.37	6.0	1.679
3	254 (10 in)	100	3.2	1.88	7.6	1.280
4	254 (10 in)	140	3.2	1.31	10.2	0.839

Table 7 Burst pressure predictions for Al-2014 cylinders with large deformation

Cylinder	Diameter (mm)	Crack Length 2a (mm)	Thick t (mm)	P_{MAX} (MPa)	Crack Growth at Pmax Δa (mm)	P_{INIT} (MPa)
3	254 (10 in)	100	3.2	1.83	7.6	1.253
4	254 (10 in)	140	3.2	1.29	11.4	0.816
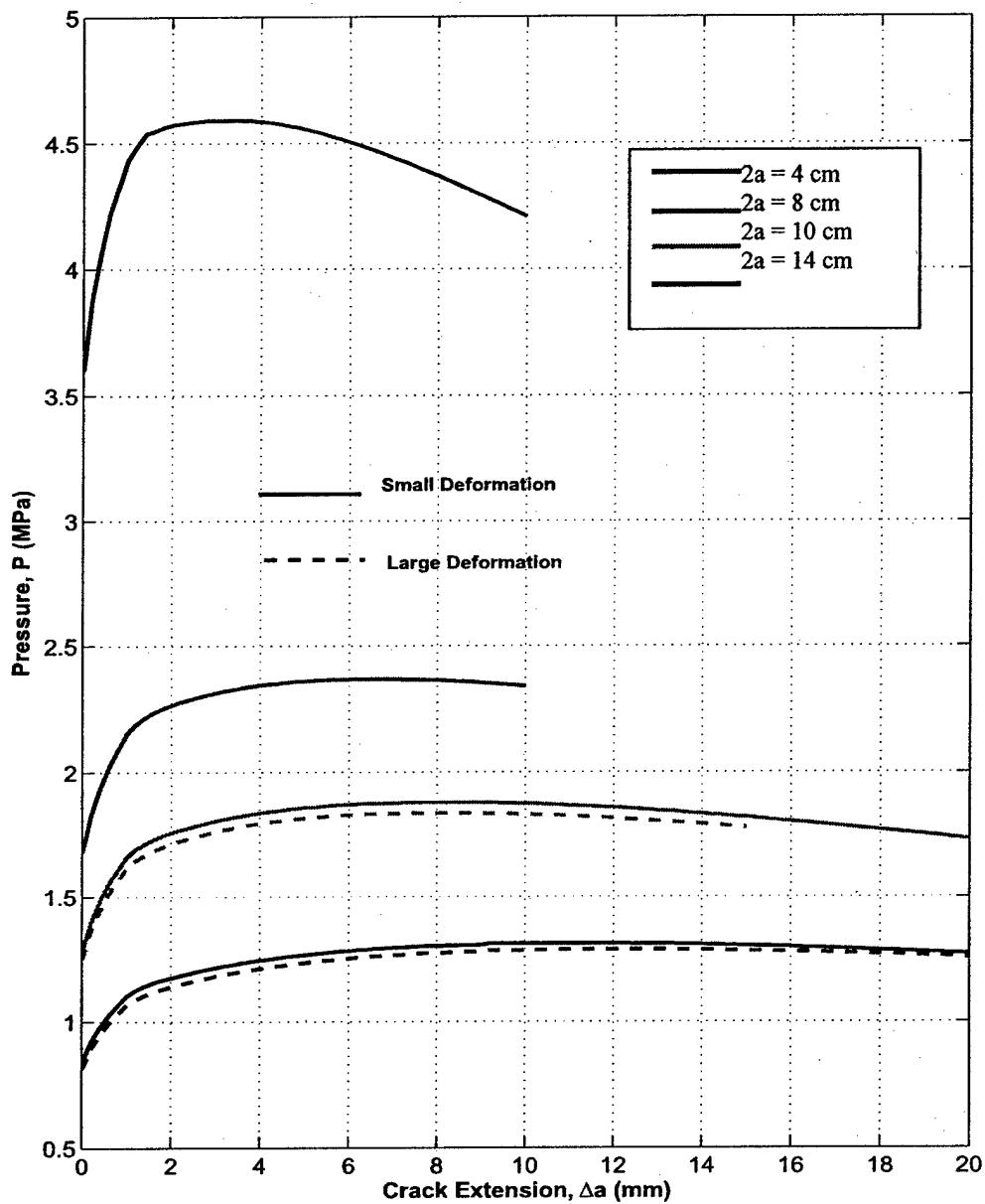
Fig. 24 Crack history data for the four Al-2014 cylinders

2.5 A Sensitivity Study

In view of the scatter in CTOA data, it is desirable to evaluate the effect of the variation in the CTOA curve on the prediction of burst pressures. With this in mind, we modified the aluminum CTOA curve by basically lowering the initial section of the fit by ignoring a few of the initial nonlinear points. Figure 25 shows the modified curve as well as the original curve. Using the original and modified CTOA curves the simulation was

performed with the result shown in Fig. 26. For comparison, the result obtained based on the constant CTOA of 5.74° is also included in the figure. It is evident that the modified CTOA curve gives results between that of the original CTOA curve and the constant CTOA assumption. There is a substantial deviation produced by the constant CTOA criterion.
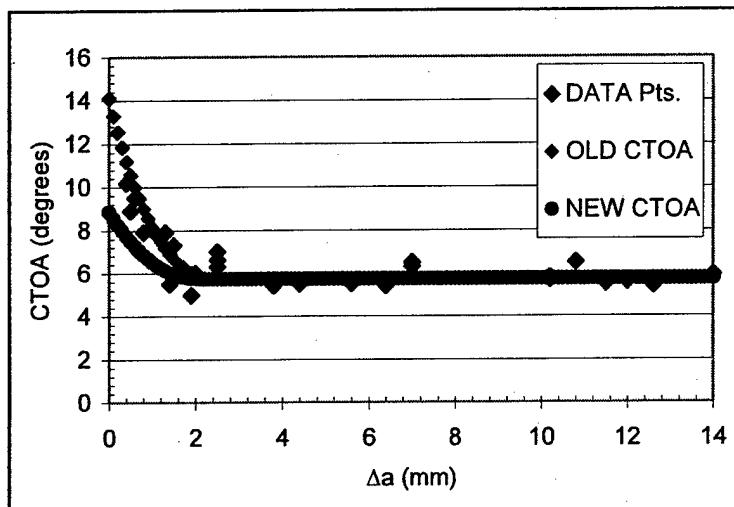
Figure 25 Modified (new) and original (old) CTOA curves for Aluminum 2014-T6
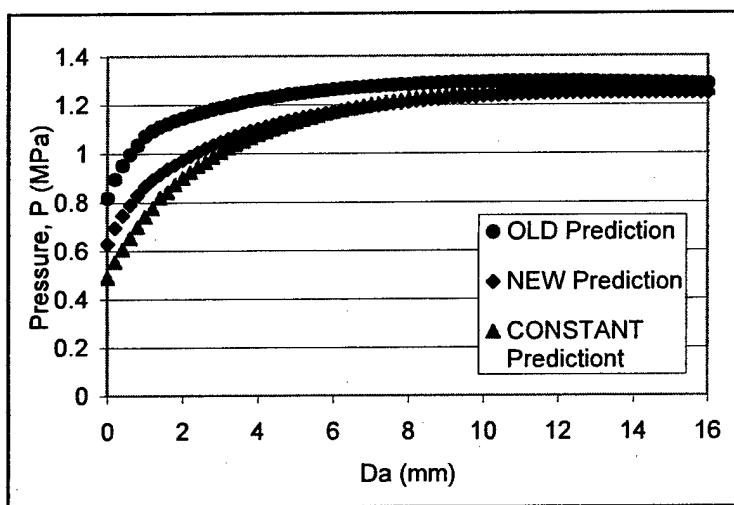
Fig. 26 Simulation result with different CTOA curves

2.6 Simulation of Burst of Aluminum Cylinders at High Temperature

38

The algorithm for determining the burst pressure of the cylinders with high temperature applied is basically the same as that outlined for the room temperature cylinder predictions. The major exception is that now the temperature of the body at each crack tip location must be used to specify which CTOA curve should be used to drive the crack propagation. This temperature tracking was done easily due to the temperature fields being clearly predefined with exact dimensions while preparing the FEA models.

The Aluminum high temperature was set at 400°C and then transitioned in 1cm/100°C fields down to room temperature of 20°C. The correct CTOA curve was then selected based on the crack extension measurement (Δa) as the crack propagated through the desired temperature fields. The remainder was discussed previously for the room temperature case.

The steps taken to apply the temperature in ABAQUS are as follows. A small pressure is applied initially to open the crack a small distance and then the temperature is increased to allow thermal strains to develop within the model. The first crack tip opening angle is then checked and the load is increased as needed to reach the critical opening angle.

The steps were done in this order to prevent the crack faces from overlapping with the imaginary other half of the crack face. Because this is not physically probable a small initial pressure was applied to prevent this. A comparison was done to determine if there was a difference in the burst pressure by applying either the temperature or small pressure first and it made none due to the pressure loading still being elastic in nature so the outlined steps were retained.

The crack dimensions were those used for the room temperature Aluminum cylinder. The crack was assumed to begin at the boundary between 200°C and 100°C with the crack tip node being 100°C for all crack lengths. The high temperature is 400°C for all but the 4cm crack length cylinders. The highest temperature used for the 2a = 4cm crack cylinder was 300°C because there wasn't room to have a 400°C zone and still begin the crack tip at the same location as the other three cylinders and retain the 1cm transition zones all at the same time.

The crack history results of these tests indicate that the heated zone increases the burst pressure of the cylinders as shown in Fig. 27. Table 8 also lists the burst pressures and the percentage that this increased for each crack length for the room temperature predictions of burst pressure, and is also shown in Fig. 28.

Table 8 Variation in burst pressure by high temperature application

2a (cm)	RT Pressure (MPa)	HT Pressure (MPa)	%change
4	4.620	4.664	0.96
8	2.341	2.425	3.58
10	1.848	1.953	5.66
14	1.296	1.412	9.00
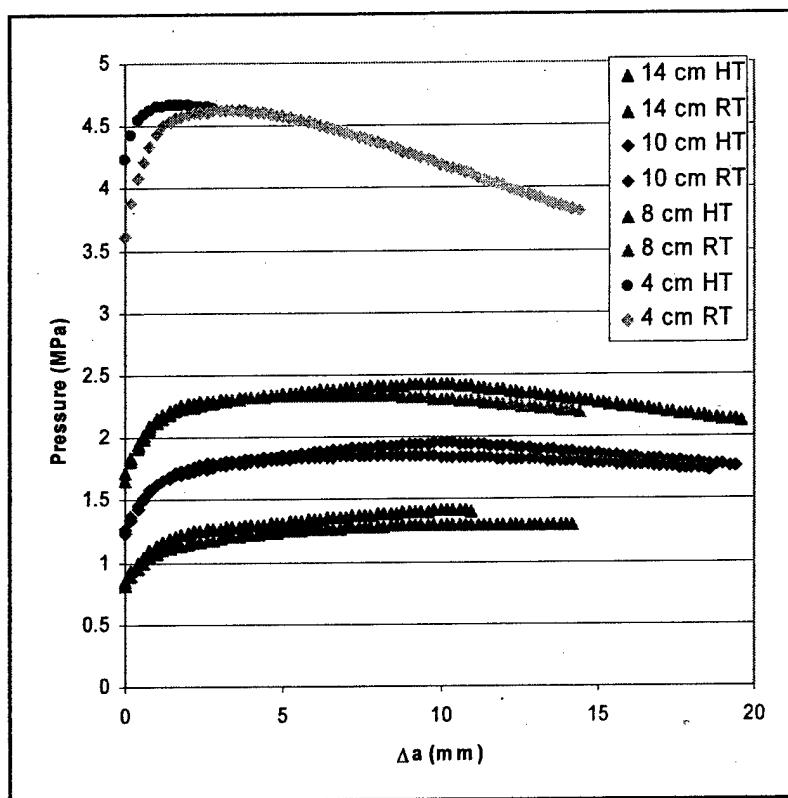
Figure 27 Crack history data for high temperature 10cm diameter Al-2014-T6 cylinders
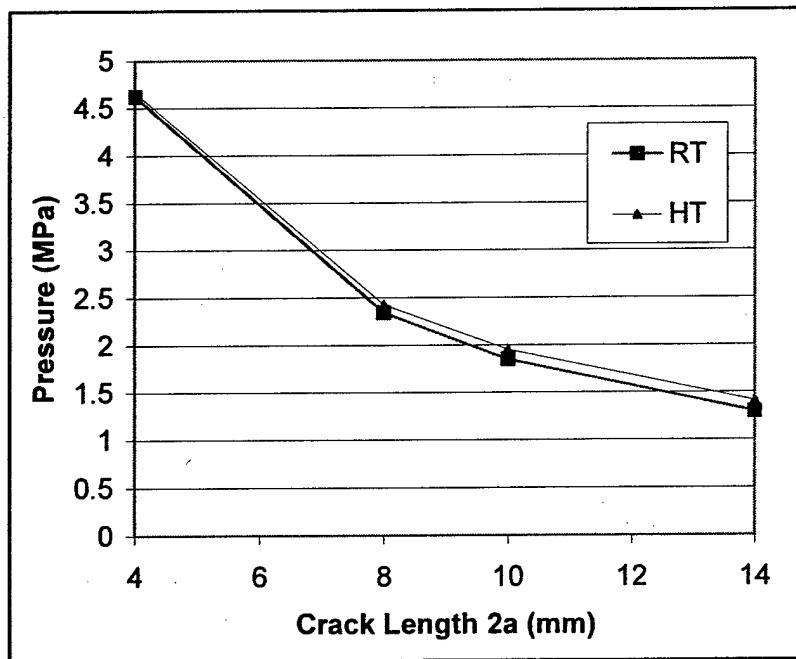
Figure 28 Burst pressure at different initial crack lengths increases with high temperature

40

A study was also done for the 2a = 4cm crack length to show how the burst pressure varied with initial condition. This case was chosen due to its higher sensitivity to changes in the initial conditions than the longer crack lengths. The premise of this study was to observe how the selection of the initial crack tip position with respect to the high temperature fields would vary the final outcome in terms of the burst pressure.

This was undertaken by applying a high temperature field at the center of the crack in a circular region to resemble the heated zone of a high energy laser. The crack was then assumed to have come into existence at some initial length, 4 cm for the study, with the crack tip resting at the boundary of some high temperature region. The boundaries between reducing temperature transition fields were required to be 1cm per 100°C drop in temperature from highest to lowest temperature as determined by AFRL. This gives for the worst case scenario for this sensitivity study a 1cm high temperature region of 400°C and then three 1cm transition zones of 300°C, 200°C, 100°C until reaching room temperature of 20°C. Because of symmetry and the length of the transition zones the crack tip will then rest between 300°C and 200°C and is assumed to be 200°C at the beginning of analysis.

For the 4cm initial crack length cylinder there are 5 different zones which can be varied by temperature increasing or decreasing the size and severity of the heated area. The crack length remains constant. The different cases considered in terms of the five temperature regions were as follows.
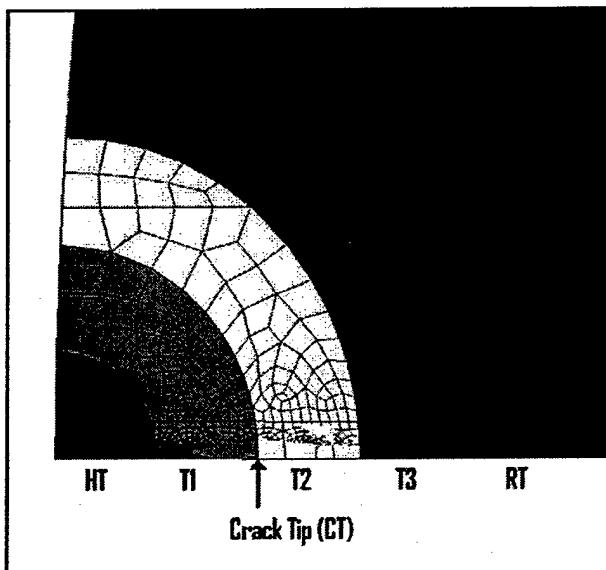
Case X: HT, T1, T2, T3, RT

Case 1:   20, 20, 20, 20, 20
Case 2:   100, 20, 20, 20, 20
Case 3:   200, 100, 20, 20, 20
Case 4:   300, 200, 100, 20, 20
Case 5:   400, 300, 200, 100, 20

Case 6:   100, 100, 20, 20, 20
Case 7:   100, 100, 100, 20, 20
Case 8:   200, 200, 100, 20, 20
Case 9:   300, 300, 200, 100, 20

Figure 29 High temperature fields used for cylinder

The overall outcome is that high temperature affects an increase in burst pressure for those cases where the crack tip is assumed to lie at 100°C or less as can be seen in Fig. 30, and that it decreases it for those where the crack tip is located at 200°. Some explanations for this trend are in the material properties of Al-2014 at elevated temperature. One is that the strength of Al-2014 at 100°C is 98% that of the room temperature material while the Crack Tip Opening Angle increases due to the rise in temperature (Fig. 16). An increase in CTOA relates to an increase in required pressure to break the cylinder, at constant temperature, and the decrease in tensile properties is not great enough to make it much easier to reach the critical opening angle required by the increased CTOA curve. The second reason the burst pressure increases is that the thermal expansion of the material acts to close the crack increasing the pressure required to reach the critical CTOA. Therefore the burst pressure must rise for these cases where the initial crack tip is assumed to lie at or beyond the 100°C. This rise in burst pressure can be seen in all those cases where the crack tip's temperature is at or greater less than 100°C. This temperature increase not being greater than 5% for any of the seven cases indicates that this doesn't greatly affect the final burst pressure, as shown in Table 9. However, in the case of the tip assumed to be at the 200°C point the CTOA is increased even greater than the 100°C curve but the tensile material properties are now 90% of room temperature and this decrease allows the material to be compliant enough to reach the critical angle at a lesser pressure than the cases with a smaller temperature loading. This is then translated throughout the entire stable crack growth and results in a decreased burst pressure for those cases with crack tips at 200°C. The change here is a more significant 12 percent drop in burst pressure for a crack developing through, Case 5, for example. This can possibly be thought of as effectively increasing the initial crack length by some Δa, which is a function of the temperature loading which could be correlated to the room temperature crack length that gives the equivalent burst pressure creating an equivalent high temperature crack length correction for structures under thermal stress.

This analysis suggests that an initial defect would quickly form through the high temperature field having crack tips at the boundary of or inside the high temperature transition field. That is what was assumed in the results given previously in Table 8. The crack was assumed to have formed with crack tips laying at the boundary between the 200°C and 100°C temperature fields where the toughness is assumed great enough to arrest the initial crack growth until high temperature and pressure is applied and then the FEA was performed to predict the failure pressure of this existing crack using the crack tip opening angle as the fracture criteria. Laboratory testing should be done to determine where the assumed crack tips would actually lie in the high-temperature/transition field so as to use the most realistic initial conditions possible for subsequent simulation work.

Table 9 Al-2014 Cylinder with 2a = 4cm burst pressure CTOA fracture prediction due to variation in thermal loading

| CASE	P_{max} (MPa)	P_{init} (MPa)	% RT P_{max} Change
Initial Crack Tip at 20°C (Fig. 23)			
1: Room Temp	4.6195	3.609	0.0
2: 100, 20, 20, 20, 20	4.645	3.663	0.6
6: 100, 100, 20, 20, 20	4.813	4.045	4.2
3: 200, 100, 20, 20, 20	4.7955	4.077	3.8
Initial Crack Tip at 100°C			
7: 100, 100, 100, 20, 20	4.7016	3.909	1.8
8: 200, 200, 100, 20, 20	4.768	4.362	3.2
4: 300, 200, 100, 20, 20	4.664	4.239	1.0
Initial Crack Tip at 200°C			
5: 400, 300, 200, 100, 20	4.072	3.382	-11.9
9: 300, 300, 200, 100, 20		3.572	
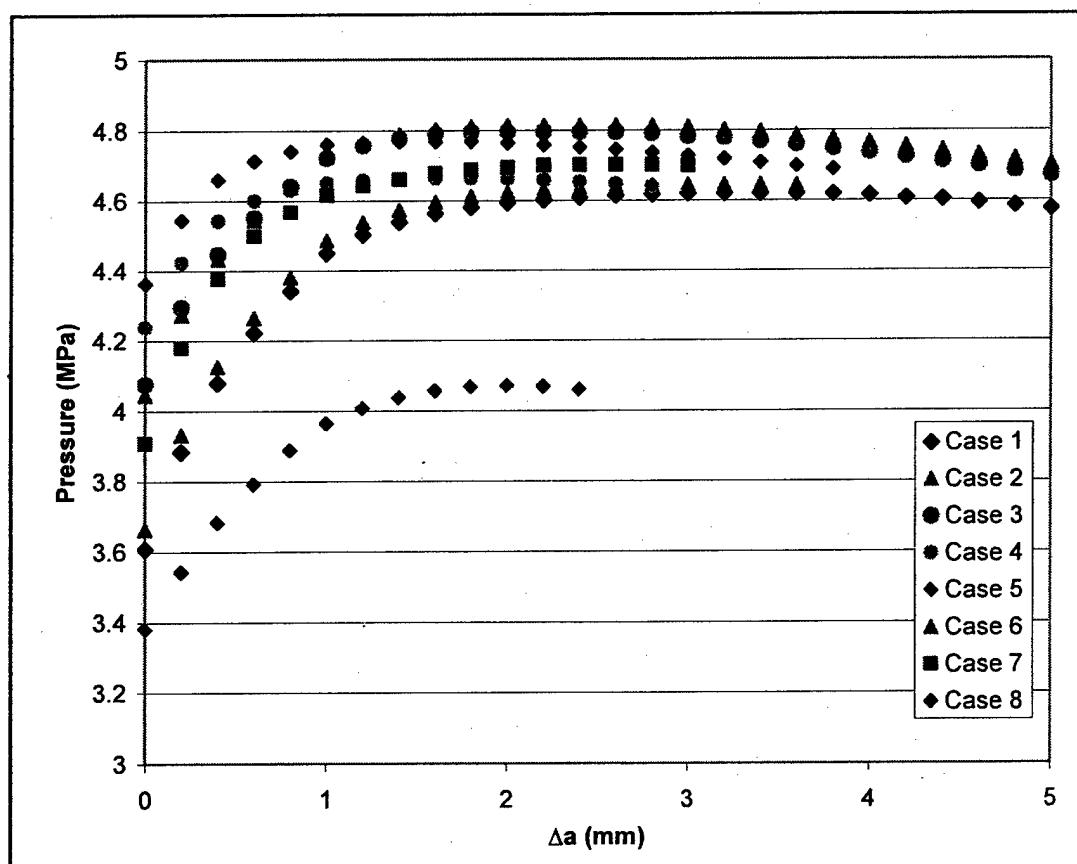
Figure 30 Al-2014-T6 cylinder with crack (2a=4cm), Pressure vs. Crack Extension High Tem

43

Part III The Development of DL Model

The Damage Length (DL) model has proven convenient and reasonably accurate in predicting failure of axially cracked cylindrical shells subjected to internal pressure. In the development of early DL models (Peters and Kuhn, 1957; Duffy et al., 1965; Anderson and Sullivan, 1966; Hahn et al., 1969; Kiefner et al., 1973), a geometrical correction factor, M, was introduced in the failure criterion for cracked flat plates to take the curvature effect into the account, and corrections to the crack length were introduced to account for the effects of plastic deformation around the crack in ductile pressure vessels with short and medium cracks. Also, the flow stress in the strip plastic zone was empirically selected. Although these studies used different geometrical and plasticity correction factors, they reported reasonable agreement between the model predictions and the experimental data of the failure hoop stress.

As these early DL models in the above studies are based on the flat plate results with empirical geometrical and plasticity corrections, Sun et al. (2003) proposed a refined DL model for pressurized thin-walled cylinders based on a sound fracture mechanics foundation. In particular, their work directly used the numerical results of Erdogan and Ratwani (1972) for an axially cracked cylindrical shell with a strip plastic zone to obtain an approximate formula for the crack tip opening displacement (CTOD). The flow stress in the strip plastic zone was determined based on an energy equivalence argument considering the strain hardening behavior of the cylinder material without resorting to experimental calibrations. The failure hoop stress and the burst pressure were evaluated using an effective stress intensity approach and the critical effective stress intensity, K_c, is determined using a ductile fracture criterion combined with finite element simulation of fracture in cylinders based on the experimentally measured CTOA data. The predicted results of the refined DL model agree with the existing experimental data for steel and aluminum cylinders, and are also in agreement with the recent test data for the four duplex steel cylinders conducted in the AFRL/DELE.

The present work aims to further improve the refined DL model for pressurized thin-walled cylinders undergoing large deflection along the crack surface and subjected to localized heating. Axially cracked thin-walled cylinders under internal pressure may experience large deflection, especially along the crack flank. In the framework of elasticity, the computational results of Rose et al. (1999) show that the stress intensity factor is reduced by the large deflection effect, which implies an increased burst pressure for the cracked shell. The present modification for the DL model to include large deflection effects is based on the arguments that large deflection effects are local around the crack and the membrane stress induced by the large deflection causes compression in the strip plastic zone, which is equivalent to the enhancement of the flow stress.

Thin-walled cylinders may be subjected to localized heating in some applications. Primary failure modes of these cylinders include the fracture along the axial direction and crack deflection along the boundary between the heated and room temperature zones. In both cases, the fracture is initiated within the heated zone as an axial crack. The present modification for the DL model to include the localized heating effects consists of

44

evaluating the thermal stress induced by the localized heating, incorporating the thermal stress effects in the calculation of fracture parameters, and the tentative consideration of crack turning along the boundary between the heated and room temperature zones.

1. Review of the Early DL Models

The early DL models (Peters and Kuhn, 1957; Duffy et al., 1965; Anderson and Sullivan, 1966; Hahn et al., 1969; Kiefner et al., 1973) predict the failure of cracked cylindrical shells based on the theory for flat plates with some empirical geometrical and plasticity corrections. For a cracked infinite plate subjected to remote tension, the failure tensile stress, σ^*, is determined by the linear elastic fracture mechanics as follows

$$\sigma^* = \frac{K_c}{\sqrt{\pi a}} \tag{3.1}$$

where K_c is the fracture toughness and a is the half crack length. The early DL models introduced a geometrical correction factor, M, to the failure stress and a plasticity correction factor, $\phi = \phi(\sigma^*, \bar{\sigma})$, to the crack length in Eq. (3.1), i.e.,

$$\sigma^* \rightarrow M\sigma_H^*, \qquad a \rightarrow \phi a \tag{3.2}$$

where $\bar{\sigma}$ is the flow stress, a material property. The failure hoop stress, σ_H^*, of the cylinder (with the same material, thickness, and crack length as those of the counterpart flat plate) was then obtained as follows

$$\sigma_H^* = \frac{K_c}{\sqrt{\pi \phi a}} M^{-1} \tag{3.3}$$

Slightly different forms of the correction factors M and ϕ were used by different research groups. The M factor was mostly based on the stress intensity result of Folias (1965) for axially cracked shells under linear elastic conditions. The ϕ factor was selected based on the Dugdale (strip plastic zone) model for flat plates. Thus, ϕ also contains M since plasticity depends on the load level. Clearly, both the derivation of the failure hoop stress (Eq. (3.3)) and the determination of the correction factors M and ϕ are highly simplified. Also, the flow stress $\bar{\sigma}$ was not rigorously determined. For example, $\bar{\sigma}$ varies between yield stress and ultimate stress in Hahn et al. (1969), and was set to equal yield stress plus 10 ksi for steels by Kiefner et al. (1973).

2. Review of the Refined DL Model for Small Deflection under Isothermal Conditions

The refined DL model (Sun et al., 2003) was based on the rigorous analyses of crack tip opening displacement for an axially cracked cylindrical shell with a strip plastic zone ahead of each crack tip (Erdogan and Ratwani, 1972) and an energy equivalence

45

argument for determining the flow stress in the strip plastic zone. Consider a cylindrical shell with an axial crack, as shown in Fig. 3.1, where R is the mean radius of the shell, t is the wall thickness and $2a$ is the crack length. A strip plastic zone of length ρ develops ahead of each crack tip upon the action of the internal pressure p.
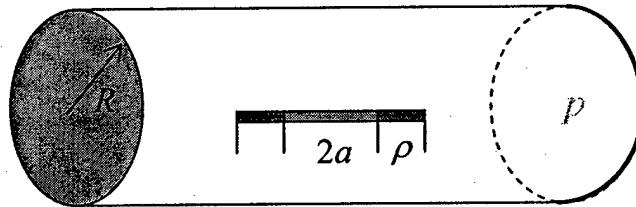
Fig. 3.1 An axially cracked cylindrical shell subjected to internal pressure

Erdogan and Ratwani (1972) solved the crack/plasticity problem using an integral transform/integral equation method and presented some graphical results for the CTOD. Sun et al. (2003) approximated the numerical results for the CTOD with the following expression

$$\delta_{tip} = -\frac{8a\beta\sigma_Y}{\pi E} \ln\left[\cos\left(\frac{\pi \sigma_H}{2 \beta\sigma_Y F_1(\lambda)} \right) \right] \tag{3.4}$$

where δ_{tip} is the CTOD, σ_H is the hoop stress, σ_Y is the yield stress, β is the ratio of the flow stress to yield stress, i.e.,

$$\beta = \frac{\bar{\sigma}}{\sigma_Y} \tag{3.5}$$

E is Young's modulus, λ is a geometrical parameter defined by

$$\lambda = \left[12\left(1 - v^2\right)\right]^{1/4} \frac{a}{\sqrt{Rt}} \tag{3.6}$$

v is Poisson's ratio, and $F_1(\lambda)$ is given by

$$F_1(\lambda) = 1/\left(1 + 0.2343\lambda + 0.2899\lambda^2\right)^{1/2} \tag{3.7}$$

The flow stress $\bar{\sigma}$, or equivalently the parameter β was determined based on an energy equivalence argument as

46

$$\beta = \frac{\overline{\sigma}}{\sigma_Y} = (N+1)^{-1/(N+1)} \left[\frac{1}{t} \left(\frac{K_c}{\sigma_Y} \right)^2 \right]^{N/(N+1)} \qquad (3.8)$$

for power-law materials (N is the hardening component), and

$$\beta = \frac{\overline{\sigma}}{\sigma_Y} = \frac{1}{2} + \frac{1}{2} \left[1 + \frac{2E_{tan}}{tE} \left(\frac{K_c}{\sigma_Y} \right)^2 \right]^{1/2} \qquad (3.9)$$

for linear-hardening materials (E_{tan} is the tangent modulus). In Eqs. (3.8) and (3.9), K_c is the effective fracture toughness.

With the determined CTOD and flow stress, Sun et al. (2003) formulated a refined DL model. They used a plasticity corrected effective stress intensity factor, K_{eff}, to predict the failure of pressurized thin-walled cylinders with an axial crack. The effective stress intensity factor, K_{eff}, is defined based on the strip plastic zone model as follows (Burdekin and Stone, 1966)

$$K_{eff} = \sqrt{E \, \overline{\sigma} \delta_{tip}} = \sqrt{E \, \beta \sigma_Y \delta_{tip}} \qquad (3.10)$$

where δ_{tip} is given in Eq. (3.4) and β is given in Eqs. (3.8) and (3.9) for power-law and linear hardening materials, respectively. Substitution of Eq. (3.4) into Eq. (3.10) yields

$$K_{eff} = \beta \sigma_Y \sqrt{\pi a} \left\{ -\frac{8}{\pi^2} \ln \left[\cos \left(\frac{\pi \, \sigma_H}{2 \, \beta \sigma_Y \, F_1(\lambda)} \right) \right] \right\}^{1/2} \qquad (3.11)$$

An argument for the above K_{eff} expression based on the J-integral concept can be found in Anderson (1995).

Assume that failure occurs when K_{eff} reaches a critical value K_c of the material (which should depend on the wall thickness), i. e.,

$$K_{eff} = K_c \qquad (3.12)$$

The failure hoop stress follows from Eqs. (3.11) and (3.12)

$$\sigma_H = \frac{2}{\pi} \beta \sigma_Y F_1(\lambda) \cos^{-1} \left\{ \exp \left[-\frac{\pi}{8a\beta^2} \left(\frac{K_c}{\sigma_Y} \right)^2 \right] \right\} \qquad (3.13)$$

Using the relationship between the hoop stress and the pressure

$$\sigma_H = (R/t)p \qquad (3.14)$$

47

the burst pressure p_{max} is obtained as follows

$$p_{\max} = \frac{2t}{\pi R} \beta \sigma_Y F_1(\lambda) \cos^{-1}\left\{\exp\left[-\frac{\pi}{8a\beta^2}\left(\frac{K_c}{\sigma_Y}\right)^2\right]\right\}$$ (3.15)

3. Development of the DL Model Including Large Deflection Effects

Both the early DL models and the refined DL model were developed in the framework of small deflection theory of shells. Axially cracked thin-walled cylinders under internal pressure, however, may experience large deflection along the crack flank. In the framework of elasticity, the computational results of Rose et al. (1999) show that the stress intensity factor is reduced by the large deflection effect, which implies an increased burst pressure for the cracked shell. The present work proposes a large deflection modification to the existing DL model for small deflections in the presence of plastic deformation. The modification is based on the arguments that large deflection of the shell wall is limited around the crack surfaces and compressive stress in the strip plastic zone may be generated due to the membrane stress induced by the large deflection, which is equivalent to the enhancement of the flow stress in the DL model.

3.1 Large Deflection Effects Modeling

It is expected that the large deflection is significant only around the crack flanks for cylindrical shells under internal pressure. We first consider an infinite plate with a central crack subjected to uniform lateral pressure, as shown in Fig. 3.2. Near the crack faces, tensile stresses are generated due to the large deflection. This tensile stress should be balanced by compressive stresses away from the crack faces. These stresses due to large deflection may induce compression ahead of the crack tip. In the DL model, this compressive stress along the crack extended line (in the strip plastic zone) may be superimposed on the flow stress due to the local nature of the large deflection. This kind of treatment of large deflections is similar to the treatment of plasticity effect around a crack in the DL model. Hence, the effect of large deflection in the DL model is reflected by the increased effective flow stress in the strip plastic zone. From this argument, we may first consider the large deflection of a cracked flat plate to obtain the additional effective flow stress due to the large deflection effect.
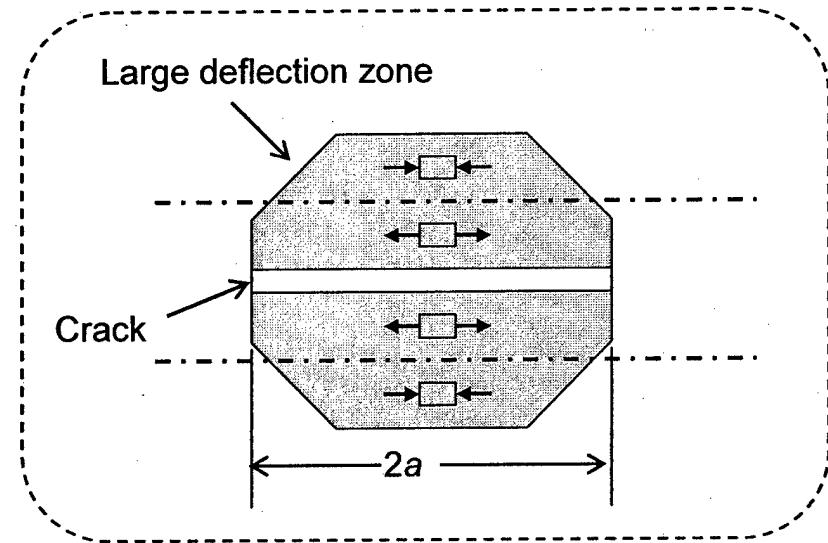
Fig. 3.2 A cracked plate subjected to lateral pressure with a large deflection zone near the crack faces

3.2 Large Deflection Induced Membrane Stress

To simplify the analyses, we consider the cylindrical bending of a plate subjected to uniform lateral pressure and clamped at the edges, as shown in Fig. 3.3. The length of the plate equals the crack length. The membrane stress due to the large deflection in this plate may be used to evaluate the stress in the cracked plate. According to the plate theory (Timoshenko, 1940), the membrane stress, σ_L, due to the large deflection is given by

$$\sigma_L = \frac{N_L}{t} = \frac{E\xi^2}{12(1-v^2)}\left(\frac{t}{a}\right)^2 \tag{3.16}$$

where N_L is the large deflection induced membrane force, E is Young's modulus, v is Poisson's ratio, t is the plate thickness, a is the half plate length (half crack length) and ξ satisfies the following nonlinear equation

$$\frac{E^2 t^8}{256(1-v^2)^2 p^2 a^8} = \frac{9}{4} \times \left(\frac{3}{\xi^8} + \frac{1}{2\xi^6} - \frac{9}{4\xi^7 \tanh(\xi)} - \frac{3}{4\xi^6 \sinh^2(\xi)}\right) \tag{3.17}$$

where p is the lateral pressure. For applications in the DL model, p should be understood as the burst pressure which is unknown yet. The membrane stress σ_L and the burst pressure p_{max} are then coupled together and in general they should be determined using a coupled, simultaneous iterative procedure. This procedure, however, may be decoupled by assuming that the pressure p in Eq. (3.17) corresponds to the burst pressure under small deflection conditions, i.e., p is given in Eq. (3.15). This assumption is not expected

to cause significant errors as a calibrated parameter will be involved in the final formulation and use of the small deflection burst pressure for p is absorbed in the calibration parameter.
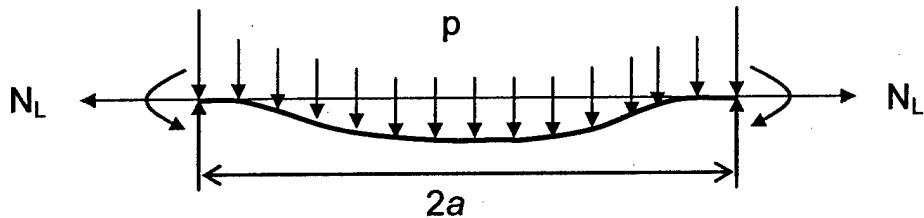
Fig. 3.3 Cylindrical bending of a plate with clamped edges (cross section view)

Eq. (3.17) now may be written in a compact form as

$$\xi = F(\xi) \tag{3.18}$$

where $F(\xi)$ is given by

$$F(\xi) = \frac{2a}{t}\left(3 + \frac{\xi^2}{2} - \frac{9\xi}{4\tanh(\xi)} - \frac{3\xi^2}{4\sinh^2(\xi)}\right)^{1/8}$$

$$\times \left(\frac{3(1-\nu^2)}{2E}\frac{2t}{\pi R}\beta\sigma_Y F_1(\lambda)\cos^{-1}\left\{\exp\left[-\frac{\pi}{8a}\left(\frac{K_c}{\beta\sigma_Y}\right)^2\right]\right\}\right)^{1/4} \tag{3.19}$$

Eq. (3.18) can be solved using a simple iterative formula

$$\xi_n = F(\xi_{n-1}), \quad n = 1, 2, \dots \tag{3.20}$$

The initial value ξ_0 can be taken as 0.01 ($\xi = 0$ for small deflection). The iteration stops when

$$\left|\frac{\xi_n - \xi_{n-1}}{\xi_{n-1}}\right| < 10^{-5} \tag{3.21}$$

and we have the approximate value $\xi = \xi_n$.

To determine the compressive stress in the strip plastic zone due to the large deflection effect, a free body diagram of the cracked plate (upper and right quarter) is considered, as depicted in Fig. 3.4, where the stresses only due to large deflection effects

50

are shown. It is assumed that the large deflection induced membrane stress in the cracked plate is nearly proportional to that given in Eq. (3.16) for the uncracked plate. The tensile stress given in Eq. (3.16) is thus adjusted for the cracked plate by a dimensionless parameter κ', which is supposed to act near the crack tip. The resultant of this tensile stress is assumed as $\kappa'\sigma_L W_1$, where W_1 is the equivalent span to which $\kappa'\sigma_L$ extends. This tensile membrane force has to be balanced by the force with equal magnitude and opposite sign away from the crack surface. The equivalent arm of the force couple is assumed to be W_2. While the large deflection induced stress is local in nature, the compressive stress is effectively distributed in the entire strip plastic zone uniformly with a magnitude of σ_{LF}. The relation between σ_{LF} and σ_L is determined by the moment balance requirement about the physical crack tip, i.e.,

$$\sigma_{LF} L \times \frac{L}{2} = \kappa'\sigma_L W_1 \times W_2 \tag{3.22}$$

where L is the length of the strip plastic zone. It follows from the above equation that

$$\sigma_{LF} = 2\kappa'\sigma_L \frac{W_1 \times W_2}{L^2} \tag{3.23}$$

The above expression may be written in a normalized form as follows

$$\sigma_{LF} = \kappa_L \left(\frac{L_{ssy}}{L}\right)^2 \sigma_L \tag{3.24}$$

where $\kappa_L = 2\kappa' W_1 W_2 / L_{ssy}^2$ needs to be calibrated using the finite element simulation result by CTOA approach, L_{ssy} is the strip plastic zone size (flat plate) under small scale yielding condition given by

$$L_{ssy} = \frac{\pi}{8}\left(\frac{K_c}{\beta\sigma_Y}\right)^2 \tag{3.25}$$

and L is

$$L = a\left\{\exp\left[\frac{\pi}{8a}\left(\frac{K_c}{\beta\sigma_Y}\right)^2\right] - 1\right\} \tag{3.26}$$

The introduction of L_{ssy} in Eq. (3.24) is for convenient purposes because L_{ssy}/L is in the interval (0, 1) and the three unknown parameters, κ', W_1 and W_2, in Eq. (3.23) can be combined into a single parameter κ_L.

51
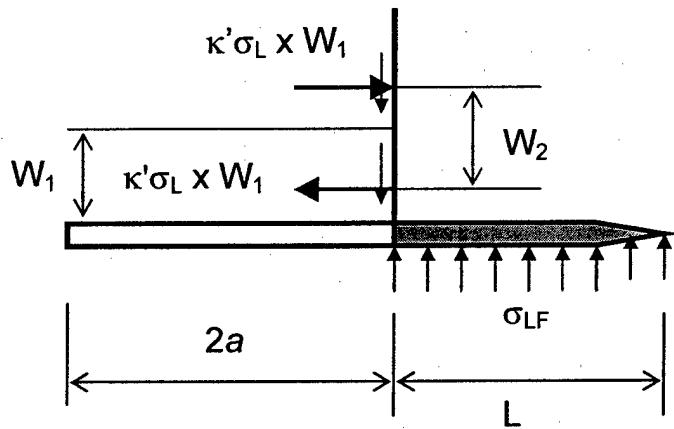
Fig. 3.4 Determination of the compressive stress in the strip plastic zone due to large deflection effect

3.3 Failure Hoop Stress and Burst Pressure

It is clear from the above discussion that the large deflection effect can be included in the DL model by adding the stress in Eq. (3.24) to the flow stress in the DL model for small deflection. The failure hoop stress in the DL model of large deflection is still given by Eq. (3.13) but with the flow stress $\beta\sigma_Y$ replaced by $\beta\sigma_Y + \kappa_L(L_{ssy}/L)^2\sigma_L$. Because the large deflection effect is local in nature, the modification of flow stress using the flat plate bending result may be adopted. We thus have the failure hoop stress in the DL model considering large deflection effects

$$\sigma_H = \frac{2}{\pi}\left[\beta\sigma_Y + \kappa_L(L_{ssy}/L)^2\sigma_L\right]F_1(\lambda)\cos^{-1}\left\{\exp\left[-\frac{\pi}{8a}\left(\frac{K_c}{\beta\sigma_Y + \kappa_L(L_{ssy}/L)^2\sigma_L}\right)^2\right]\right\} \quad (3.27)$$

and the burst pressure p_{max} is

$$p_{max} = \frac{2t}{\pi R}\left[\beta\sigma_Y + \kappa_L(L_{ssy}/L)^2\sigma_L\right]F_1(\lambda)\cos^{-1}\left\{\exp\left[-\frac{\pi}{8a}\left(\frac{K_c}{\beta\sigma_Y + \kappa_L(L_{ssy}/L)^2\sigma_L}\right)^2\right]\right\} \quad (3.28)$$

It is noted that there is a free parameter κ_L in the failure hoop stress expression (3.27) and the burst pressure (3.28). The parameter needs to be calibrated by matching the predictions from the DL model with large deformation finite element simulation results based on the CTOA criterion.

52

3.4 Numerical Results

The burst pressures are calculated for the four tested steel cylinders using Eq. (3.28). Table 3.1 lists the geometric dimensions of the cylinders. The material properties are listed in Table 3.2. Three fracture toughness values are considered.

Table 3.1 Geometric parameters of the steel cylinders

Specimen	Diameter (mm)	Crack Length $2a$ (mm)	Thickness (mm)	λ
1	254	120	1.5	7.9
2	254	90	1.5	5.9
3	254	60	1.5	4.0
4	254	30	1.5	2.0

Table 3.2 Material properties of the steel at the room temperature

Yield Strength (MPa)	Ultimate Strength (MPa)	Hardening exponent	Young's modulus (GPa)	Poisson's ratio)	Thermal expansion $(10^{-6}/\,^\circ C)$	Toughness (K_c) $(MPa\text{-}m^{1/2})$
600	910	0.056	209	0.3	12	300, 330, 392

The dimensionless parameter κ_L is first calibrated as 1.6 by matching the DL model prediction with the CTOA simulation result (large deformation) for the specimen with the longest crack length (120 mm) when the toughness is taken as 392 MPa-m$^{1/2}$. It is found that by matching the DL model result using $K_c = 330$ MPa-m$^{1/2}$ (300 ksi-in$^{1/2}$) with the CTOA result for cylinder #1, the value of κ_L is calibrated as 7.5 which leads to improved predictions. Table 3.3 lists the predictions from the DL model and the CTOA simulation, as well as the test burst pressure data using $\kappa_L = 7.5$.

Table 3.3 Burst pressure results ($K_c = 330$ MPa-m$^{1/2}$, $\kappa_L = 7.5$)

Specimen	Crack Length $2a$ (mm)	P_{MAX} (MPa) (CTOA, large deformation)	P_{MAX} (MPa) (DL, large deflection)	P_{MAX} (MPa) (DL, small deflection)	P_{MAX} (MPa) (test)
1	120	1.86	1.86	1.59	2.11
2	90	2.52	2.59	2.21	2.69
3	60	3.33	3.57	3.33	3.67
4	30	5.40	5.51	5.51	5.35

Fig. 3.5 shows the burst pressure (normalized by $p_u = \sigma_u(t/R)$, σ_u: the ultimate stress) versus the normalized crack length $\lambda^* = a/(Rt)^{1/2}$ using $K_c = 356$ ksi-in$^{1/2}$ and $\kappa_L = 7.5$. Figs. 3.6 and 3.7 show the corresponding results for $K_c = 300$ ksi-in$^{1/2}$ and $K_c = 273$

53

ksi-in$^{1/2}$, respectively. It can be seen from the figures that the burst pressures are increased for cracks with $\lambda^* > 3$ by considering large deflection effects. The DL model predictions using $\kappa_L = 7.5$ are in good agreement with the test data.
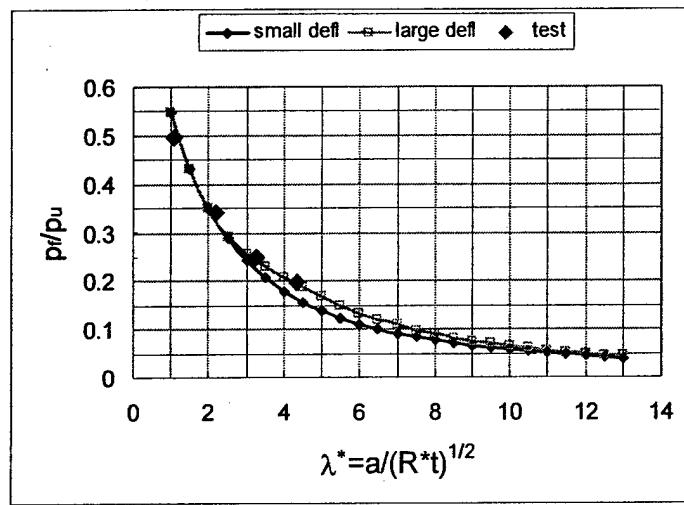
(a)
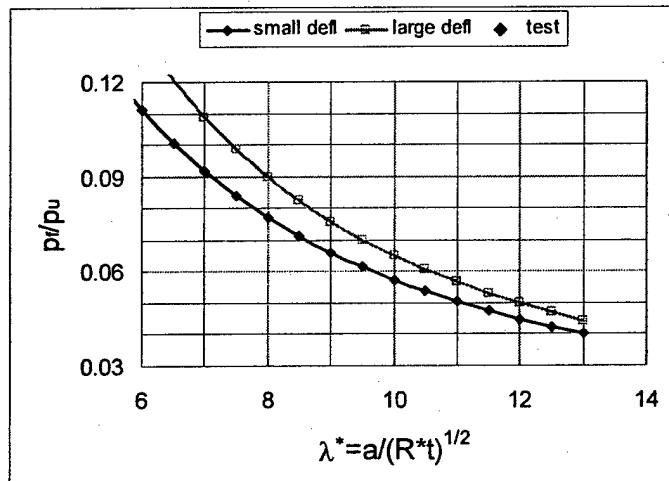
(b)

Fig. 3.5 Numerical Results: $K_c = 356$ ksi-in$^{1/2}$, $\kappa_L = 7.5$
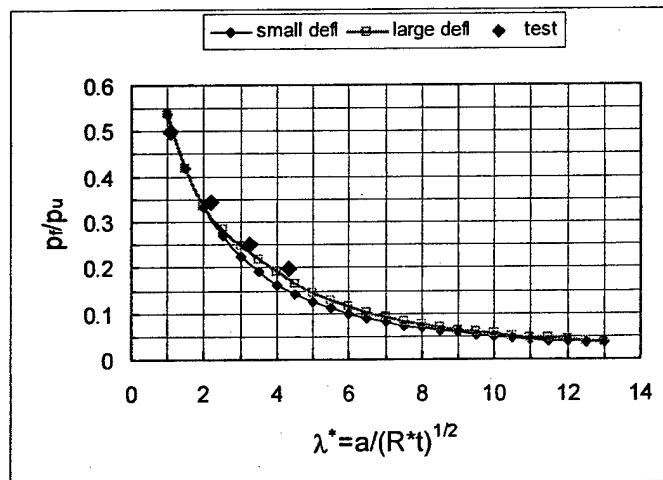
(a)
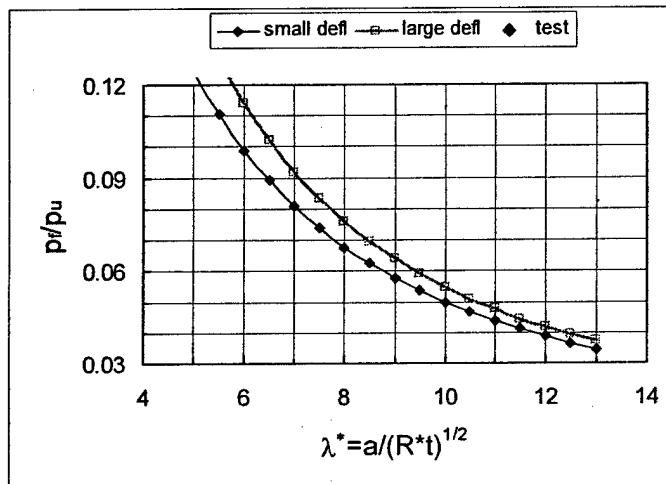
(b)

Fig. 3.6 Numerical Results: $K_c = 300$ ksi- in$^{1/2}$, $\kappa_L = 7.5$
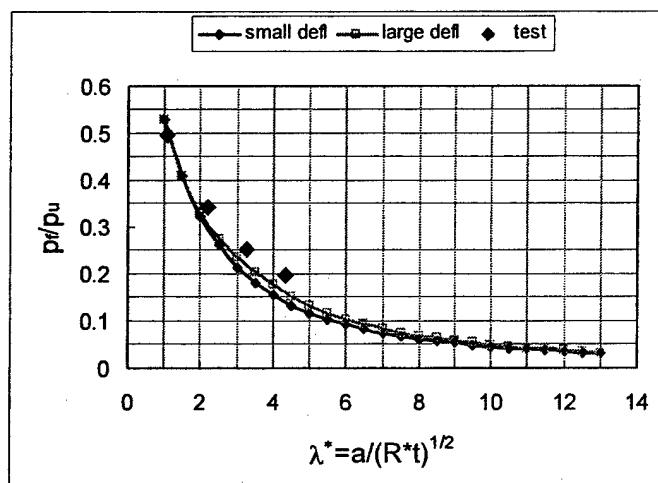
(a)
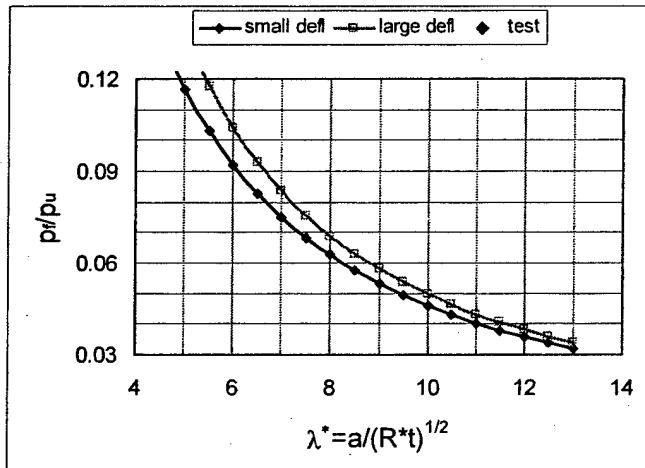
(b)

Fig. 3.7 Numerical Results: $K_c = 273$ ksi- in$^{1/2}$, $\kappa_L = 7.5$

4. Development of the DL Model Including Localized Heating Effects

Thin-walled cylinders may be subjected to localized heating in some applications. Primary failure modes of these cylinders include the fracture along the axial direction and crack deflection along the boundary between the heated and room temperature zones. In both cases, the fracture is initiated within the heated zone as an axial crack. This section first focuses on the fracture along the axial direction and derives a DL model considering the thermal stress induced by the non-uniform temperature field. Due to the difficulties to include the temperature effect in the analyses of shell structures, we follow the early DL models by first considering a cracked flat plate and then modifying the flat plate result

with the so-called M correction factor. We use the factor F_1 in the refined DL model (Eq. (3.7)) as this factor together with the flat plate formula very well approximates the shell CTOD result under isothermal conditions.

4.1 Thermal Stresses due to the Localized Heating

Consider an infinite plate subjected to uniform heating in a circular zone with a radius of ρ, as shown in Fig. 3.8. The temperature keeps at T_1 in the heated zone and is initially T_0 elsewhere. As a first order approximation, we neglect the time-dependent effect of temperature. The problem is symmetric and the thermal stresses due to the localized heating are then governed by the following equations

$$\frac{d\sigma_{rr}}{dr} + \frac{\sigma_{rr} - \sigma_{\theta\theta}}{r} = 0 \tag{3.29}$$

$$\sigma_{rr} = \frac{E_1}{1-v_1^2}\left(\varepsilon_{rr} + v_1\varepsilon_{\theta\theta}\right) - \frac{E_1\alpha_1}{1-v_1}\left(T_1 - T_0\right),$$

$$\sigma_{\theta\theta} = \frac{E_1}{1-v_1^2}\left(\varepsilon_{\theta\theta} + v_1\varepsilon_{rr}\right) - \frac{E_1\alpha_1}{1-v_1}\left(T_1 - T_0\right) \tag{3.30}$$

$$\varepsilon_{rr} = \frac{du_r}{dr}, \qquad \varepsilon_{\theta\theta} = \frac{u_r}{r} \tag{3.31}$$

in the heated zone, where σ_{rr} and $\sigma_{\theta\theta}$ are stresses, ε_{rr} and $\varepsilon_{\theta\theta}$ are strains, u_r is the radial displacement, and E_1, v_1 and α_1 are Young's modulus, Poisson's ratio and the coefficient of thermal expansion (CTE) in the heated zone (at the elevated temperature T_1), respectively. Outside the heated zone, the stresses, strains and displacement are governed by Eqs. (3.29), (3.31) and the following stress-strain relationship

$$\sigma_{rr} = \frac{E_0}{1-v_0^2}\left(\varepsilon_{rr} + v_0\varepsilon_{\theta\theta}\right),$$

$$\sigma_{\theta\theta} = \frac{E_0}{1-v_0^2}\left(\varepsilon_{\theta\theta} + v_0\varepsilon_{rr}\right) \tag{3.32}$$

where E_0, v_0 and α_0 are Young's modulus, Poisson's ratio and the CTE outside the heated zone (at the room temperature T_0), respectively. At the interface ($r = \rho$) between the heated and room temperature zones, the normal stress σ_{rr} and displacement u_r are continuous. Here we have neglected the temperature transition zone where the temperature changes continuously although precipitously. Evidently, the thermal stresses should vanish at infinity.
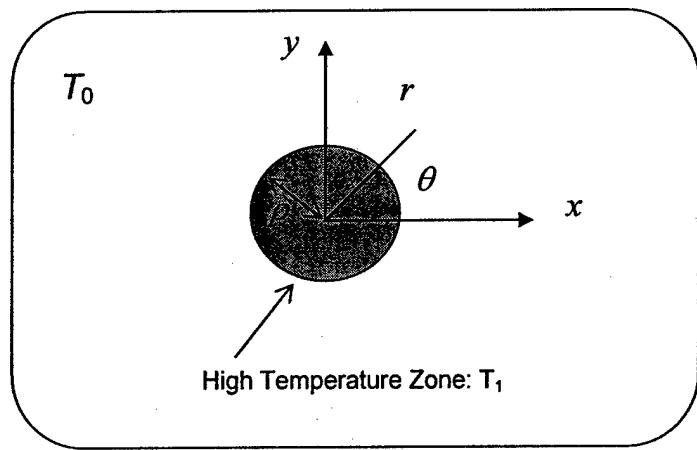
Fig. 3.8 An infinite plate subjected to localized heating in $r < \rho$

By solving the basic equations (3.29) – (3.32) and using the appropriate interface conditions, one can easily obtain the displacement and thermal stresses in the infinite plate subjected to the localized heating as follows

$$u_r = \alpha_1 (T_1 - T_0) r \Big/ \left(1 + \frac{\mu_0}{\mu_1} \frac{1 - \nu_1}{1 + \nu_1} \right) \tag{3.33}$$

$$\sigma_{rr} = -\frac{1}{2} E_0 \alpha_0 (T_1 - T_0) \left[\frac{2\alpha_1 / \alpha_0}{1 + \nu_0 + (1 - \nu_1) E_0 / E_1} \right],$$

$$\sigma_{\theta\theta} = \sigma_{rr} \tag{3.34}$$

in the heated zone ($r < \rho$), and

$$u_r = \frac{\rho^2}{r} \alpha_1 (T_1 - T_0) \Big/ \left(1 + \frac{\mu_0}{\mu_1} \frac{1 - \nu_1}{1 + \nu_1} \right) \tag{3.35}$$

$$\sigma_{rr} = -\frac{1}{2} E_0 \alpha_0 (T_1 - T_0) \left[\frac{2\alpha_1 / \alpha_0}{1 + \nu_0 + (1 - \nu_1) E_0 / E_1} \right] \left(\frac{\rho}{r} \right)^2,$$

$$\sigma_{\theta\theta} = -\sigma_{rr} \tag{3.36}$$

outside the heated zone ($r > \rho$). In Eqs. (3.33) – (3.36), μ_1 and μ_0 are the shear moduli in and outside the heated zone, respectively.

58

Fig. 3.9 shows the variation of Young's modulus with temperature for a duplex steel. The Young's modulus decreases from about 195 GPa at the room temperature to about 140 GPa at a temperature of 800^0C.
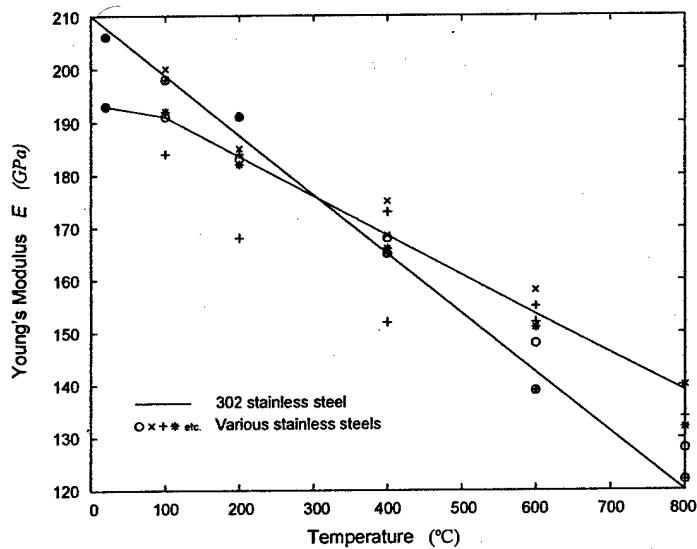
Fig. 3.9 Young's modulus variation with temperature (from the sponsor)

4.2 Crack Tip Opening Displacement

Assume there is an axial crack with a length equal to the diameter of the circular heated zone. In the DL model, we assume that a strip plastic zone develops ahead of each crack tip, as shown in Fig. 3.10, where a ($= \rho$) is the half crack length and $c - a$ is the length of the strip plastic zone. In the analysis of the crack problem, we first neglect the temperature dependence of Young's modulus, Poisson's ratio and the CTE because the heated zone is relatively small and the effect of variations in these properties may not significant. The effect of the temperature dependence of material properties on thermal stresses, however, is considered in Eqs. (3.34) and (3.36).
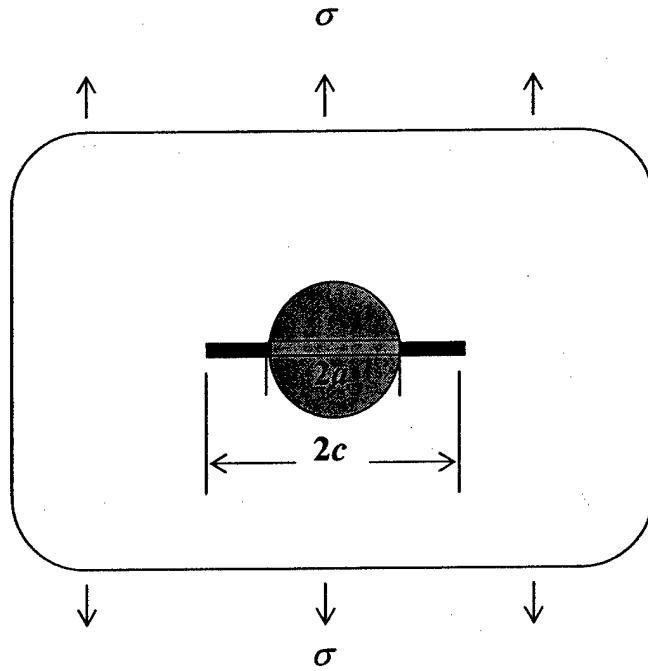
Fig. 3.10 The strip plastic zone in a cracked infinite plate subjected to localized heating

The stress singularity at the tip of the strip plastic zone should be cancelled in the DL model. We thus have

$$K_I = K_I^{appl} + K_I^{flow} + K_I^{therm} = 0 \qquad (3.37)$$

where K_I^{appl}, K_I^{flow} and K_I^{therm} are the stress intensity factors due to the applied stress, the flow stress in the strip plastic zone, and the thermal stress, respectively

$$K_I^{appl} = \sigma \sqrt{\pi c} \qquad (3.38a)$$

$$K_I^{flow} = -\frac{2\bar{\sigma}_0}{\sqrt{\pi c}} \int_a^c \frac{d\xi}{\sqrt{1-\xi^2/c^2}} = -\frac{2\bar{\sigma}_0}{\sqrt{\pi c}} c \cos^{-1}\left(\frac{a}{c}\right) \qquad (3.38b)$$

$$K_I^{therm} = -\frac{\eta E_0 \alpha_0 \Delta T}{\sqrt{\pi c}} \int_0^a \frac{d\xi}{\sqrt{1-\xi^2/c^2}} + \frac{\eta E_0 \alpha_0 \Delta T}{\sqrt{\pi c}} \int_a^c \left(\frac{a}{\xi}\right)^2 \frac{d\xi}{\sqrt{1-\xi^2/c^2}}$$

$$= \eta E_0 \alpha_0 \Delta T \sqrt{\frac{c}{\pi}} \left[-\sin^{-1}\left(\frac{a}{c}\right) + \left(\frac{a}{c}\right)\sqrt{1-\frac{a^2}{c^2}} \right] \qquad (3.38c)$$

60

where σ is the applied stress at infinity, $\bar{\sigma}_0$ is the flow stress in the room temperature zone (the plastic zone is in the room temperature zone), $\Delta T = T_1 - T_0$, and η is a bimaterial parameter given by

$$\eta = \frac{2\alpha_1 / \alpha_0}{1 + \nu_0 + (1 - \nu_1)E_0 / E_1} \tag{3.39}$$

Substituting Eq. (3.38) into Eq. (3.37), we obtain the following relation between the applied stress and the strip plastic zone length

$$\frac{\sigma}{\bar{\sigma}_0} - \frac{2}{\pi}\cos^{-1}\left(\frac{a}{c}\right) + \frac{\eta E_0 \alpha_0 \Delta T}{\pi \bar{\sigma}_0}\left[-\sin^{-1}\left(\frac{a}{c}\right) + \left(\frac{a}{c}\right)\sqrt{1 - \frac{a^2}{c^2}}\right] = 0 \tag{3.40}$$

The above equation reduces to that of the Dugdale model when the plate is under isothermal conditions (i.e., $\Delta T = 0$).

We now evaluate the crack tip opening displacement at the physical crack tip (CTOD). The total CTOD is given by

$$\delta_{tip} = \delta_{tip}^{appl} + \delta_{tip}^{flow} + \delta_{tip}^{therm} \tag{3.41}$$

where δ_{tip}^{appl}, δ_{tip}^{flow} and δ_{tip}^{therm} are the CTODs due to the applied traction, the flow stress, and the thermal stress, respectively

$$\delta_{tip}^{appl} = \frac{4\sigma}{\pi E_0}\int_0^c G(a,\xi)d\xi = \frac{4c\sigma}{E_0}\sqrt{1 - \frac{a^2}{c^c}} \tag{3.42a}$$

$$\delta_{tip}^{flow} = -\frac{4\bar{\sigma}_0}{\pi E_0}\int_a^c G(a,\xi)d\xi = -\frac{8c\bar{\sigma}_0}{\pi E_0}\left[\sqrt{1 - \frac{a^2}{c^2}}\cos^{-1}\left(\frac{a}{c}\right) + \frac{a}{c}\ln\left(\frac{a}{c}\right)\right] \tag{3.42b}$$

$$\delta_{tip}^{therm} = \frac{2\eta E_0 \alpha_0 \Delta T}{\pi E_0}\left[-\int_0^a G(a,\xi)d\xi + \int_a^c \left(\frac{a}{\xi}\right)^2 G(a,\xi)d\xi\right]$$

$$= -\frac{4c\eta \alpha_0 \Delta T}{\pi}\sqrt{1 - \frac{a^2}{c^2}}\sin^{-1}\left(\frac{a}{c}\right), \tag{3.42c}$$

where $G(a,\xi)$ is a function given by

$$G(x,\xi) = \ln\left|\frac{\sqrt{c^2 - x^2} + \sqrt{c^2 - \xi^2}}{\sqrt{c^2 - x^2} - \sqrt{c^2 - \xi^2}}\right|$$

Substituting Eqs. (3.42) into Eq. (3.41), we obtain the total CTOD after lengthy mathematical manipulations

$$\delta_{tip} = \frac{8a\bar{\sigma}_0}{\pi E_0}\left[\ln\left(\frac{c}{a}\right) - \frac{\eta E_0 \alpha_0 \Delta T}{2\bar{\sigma}_0}\left(1 - \frac{a^2}{c^2}\right)\right] \qquad (3.43)$$

In the above derivations, it is assumed that the material in the heated zone deforms elastically. If plastic yielding occurs in the hot spot due to the severe thermal stress effect, the thermal stress term in Eqs. (3.40) and (3.43), i.e., $\eta E_0 \alpha_0 \Delta T / 2$, may be approximately replaced by the smaller of σ_{YT} and $\sigma_Y / \sqrt{3}$, where σ_{YT} and σ_Y are the yield stresses at the high temperature in the hot spot and at the room temperature, respectively.

The above derived CTOD (Eq. (3.43)) and the strip plastic zone length (Eq. (3.40)) are for a cracked infinite flat plate. For an axially cracked cylinders subjected to localized heating as shown in Fig. 3.11, we introduce a correction factor $F_1(\lambda)$ to modify the applied traction as in the early DL models (e.g., Hahn et al. (1969) and Kiefner et al. (1973)) and the same correction factor is also used to modify the thermal stress for CTOD calculations. This thermal stress itself, however, is for flat plates and should also be corrected for cylinders. That is to say, the thermal stresses in Eqs. (3.34) and (3.36) should be corrected twice: the first correction is to obtain the thermal stress in cylinders, and the second is in the calculation of CTOD. According to the descriptions in Timoshenko (1940), the thermal stress in the hot spot of the cylinder may be assumed as having the following form

$$\sigma_{\theta\theta} = -\frac{1}{2}E_0\alpha_0\left(T_1 - T_0\right)\eta \times \kappa_T F_1(\lambda)$$

where $F_1(\lambda)$ is given in Eq. (3.7) with λ defined in Eq. (3.6) and κ_T is a correction coefficient to be calibrated by CTOA simulation results or experiments. Hence, Eqs. (3.40) and (3.43) become for cylinders

$$\frac{\sigma_H}{\bar{\sigma}_0 F_1(\lambda)} - \frac{2}{\pi}\cos^{-1}\left(\frac{a}{c}\right) - \frac{\eta E_0 \alpha_0 \Delta T \kappa_T F_1(\lambda)}{\pi\bar{\sigma}_0 F_1(\lambda)}\left[\sin^{-1}\left(\frac{a}{c}\right) - \left(\frac{a}{c}\right)\sqrt{1 - \frac{a^2}{c^2}}\right] = 0 \qquad (3.44)$$

$$\delta_{tip} = \frac{8a\bar{\sigma}_0}{\pi E_0}\left[\ln\left(\frac{c}{a}\right) - \frac{\eta E_0 \alpha_0 \Delta T \kappa_T F_1(\lambda)}{2\bar{\sigma}_0 F_1(\lambda)}\left(1 - \frac{a^2}{c^2}\right)\right] \qquad (3.45)$$
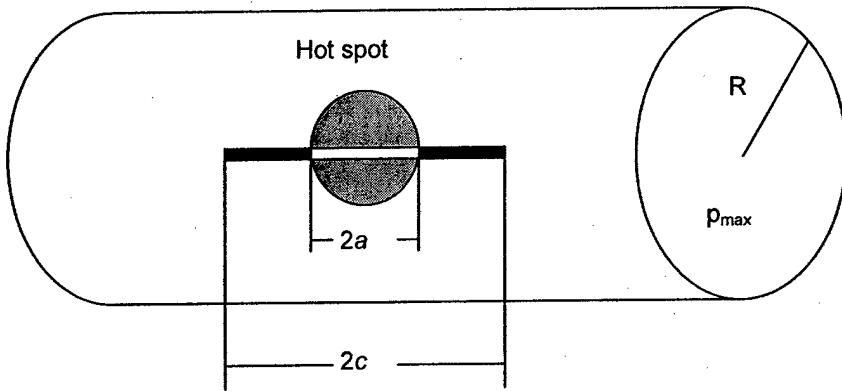
Fig. 3.11 An axially cracked cylindrical shell subjected to localized heating

Because the strip plastic zone is in the room temperature zone, the flow stress can be determined based on the room temperature properties, i.e.,

$$\overline{\sigma}_0 = \beta_0 \, \sigma_Y^0 \qquad (3.46)$$

where σ_Y^0 is the yield stress in the room temperature zone and β_0 is given by

$$\beta_0 = \frac{\overline{\sigma}_0}{\sigma_Y^0} = \left(N_0 + 1\right)^{-1/(N_0+1)} \left[\frac{1}{t}\left(\frac{K_c^0}{\sigma_Y^0}\right)^2\right]^{N_0/(N_0+1)} \qquad (3.47)$$

for power-law materials, and

$$\beta_0 = \frac{\overline{\sigma}_0}{\sigma_Y^0} = \frac{1}{2} + \frac{1}{2}\left[1 + \frac{2E_{tan}^0}{tE_0}\left(\frac{K_c^0}{\sigma_Y^0}\right)^2\right]^{1/2} \qquad (3.48)$$

for linear-hardening materials. In Eqs. (3.47) and (3.48), N_0 is the hardening exponent, E_{tan}^0 is the tangent modulus and K_c^0 is the fracture toughness at the room temperature, respectively.

4.3 Failure Hoop Stress and Burst Pressure

Under isothermal conditions, Sun et al. (2003) used a plasticity corrected effective stress intensity factor, K_{eff}, to predict the failure hoop stress and burst pressure. Under the localized heating conditions, the effective stress intensity factor, K_{eff}, can still be defined based on the strip plastic zone model as follows (Burdekin and Stone, 1966)

63

$$K_{eff} = \sqrt{E_0 \, \overline{\sigma}_0 \delta_{tip}} = \sqrt{E_0 \, \beta_0 \sigma_Y^0 \delta_{tip}} \tag{3.49}$$

where the material properties are taken at the room temperature. The failure criterion can thus be described by

$$K_{eff} = K_c^0 \tag{3.50}$$

where K_c^0 is the fracture toughness at room temperature. Substituting Eq. (3.49) into Eq. (3.50) and using Eq. (3.45), we get the following relation

$$\ln\left(\frac{c}{a}\right) - \frac{\kappa_T \eta E_0 \alpha_0 \Delta T}{2\beta_0 \sigma_Y^0}\left(1 - \frac{a^2}{c^2}\right) = \frac{\pi E_0 \delta_c^0}{8a\beta_0 \sigma_Y^0} \tag{3.51}$$

where δ_c^0 is related to K_c^0 by

$$K_c^0 = \sqrt{E_0 \, \beta_0 \sigma_Y^0 \delta_c^0} \tag{3.52}$$

Eq. (3.51) determines the size of the strip plastic zone c/a which depends on ΔT. The failure hoop stress is obtained from Eq. (3.44)

$$\sigma_H = \frac{2}{\pi}\beta_0 \sigma_Y^0 F_1(\lambda)\left\{\cos^{-1}\left(\frac{a}{c}\right) + \frac{\kappa_T \eta E_0 \alpha_0 \Delta T}{2\beta_0 \sigma_Y^0}\left[\sin^{-1}\left(\frac{a}{c}\right) - \left(\frac{a}{c}\right)\sqrt{1 - \frac{a^2}{c^2}}\right]\right\} \tag{3.53}$$

Using the relationship between the hoop stress and the pressure (3.14)

$$\sigma_H = (R/t)p$$

we obtain the burst pressure p_{max} as follows

$$p_{max} = \frac{2t}{\pi R}\beta_0 \sigma_Y^0 F_1(\lambda)\left\{\cos^{-1}\left(\frac{a}{c}\right) + \frac{\kappa_T \eta E_0 \alpha_0 \Delta T}{2\beta_0 \sigma_Y^0}\left[\sin^{-1}\left(\frac{a}{c}\right) - \left(\frac{a}{c}\right)\sqrt{1 - \frac{a^2}{c^2}}\right]\right\} \tag{3.54}$$

Eqs. (3.51), (3.53) and (3.54) indicate that the failure hoop stress and the burst pressure are affected by the geometrical parameters of the cylinder, crack length, fracture toughness, yield stress, strain-hardening behavior (through parameter β_0) and the temperature difference ΔT. When $\Delta T = 0$, the formulas reduce to those under isothermal conditions.

4.4 Numerical Results

64

The burst pressures are tentatively calculated for the four tested (under constant temperature) steel cylinders using Eqs. (3.51) and (3.54) for a temperature rise of $\Delta T = 1000°C$. Table 3.4 lists the material properties of the steel at the room temperature. The toughness (K_c) value is taken as 392 MPa-m$^{\frac{1}{2}}$ (356 ksi-in$^{\frac{1}{2}}$).

Table 3.4 Material properties of the steel at the room temperature

Yield Strength (MPa)	Ultimate Strength (MPa)	Hardening exponent	Young's modulus (GPa)	Poisson's ratio)	Thermal expansion $(10^{-6}\,°C^{-1})$	Toughness (K_c) $(MPa\text{-}m^{1/2})$
600	910	0.056	209	0.3	12	392

The material properties at 1000°C are unknown at the present time. The estimated values of Young's modulus, Poisson's ratio and the CTE (which are needed in the current model) are listed in Table 3.5.

Table 3.5 Material properties of the steel at 1000°C

Yield Strength (MPa)	Ultimate Strength (MPa)	Hardening exponent	Young's modulus (GPa)	Poisson's ratio)	Thermal expansion $(10^{-6}\,°C^{-1})$	Toughness (K_c) $(MPa\text{-}m^{1/2})$
			110	0.3	20	

The pressure results are listed in Table 3.6. The correction coefficient κ_T is tentatively chosen as 1.0 and should be calibrated in the future work. It can be seen from the table that the burst pressure is only slightly increased by the consideration of the thermal stress effect due to the localized heating.

Table 3.6 Burst pressure results (small deflection)

Specimen	Diameter (mm)	Crack Length 2a (mm)	P_{MAX} (MPa) (room temperature)	P_{MAX} (MPa) ($\Delta T = 1000°C$)
1	254 (10 in)	120	1.75	1.84
2	254 (10 in)	90	2.39	2.45
3	254 (10 in)	60	3.50	3.53
4	254 (10 in)	30	5.63	5.64

5. The DL Model under Combined Large Deflection and Localized Heating Conditions

Generally speaking, a coupled approach is needed to simultaneously consider the combined effects of large deflection and thermal stress due to localized heating. A first attempt is to use an uncoupled approach and the effect of coupling is lumped into the calibration parameter κ_L for large deflection. Hence, the large deflection effect is taken

into account by adding the large deflection induced stress $\kappa_L \left(L_{ssy}^0 / L_0 \right) \sigma_L^1$ to the flow stress $\beta_0 \sigma_Y^0$ in Eq. (3.54), the burst pressure for small deflection under isothermal conditions. The burst pressure now can be calculated from

$$p_{max} = \frac{2t}{\pi R} \left[\beta_0 \sigma_Y^0 + \kappa_L (L_{ssy}^0 / L_0)^2 \sigma_L^1 \right] F_1(\lambda)$$

$$\times \left\{ \cos^{-1}\left(\frac{a}{c} \right) + \frac{\kappa_T \eta E_0 \alpha_0 \Delta T}{2 \left[\beta_0 \sigma_Y^0 + \kappa_L (L_{ssy}^0 / L_0)^2 \sigma_L^1 \right]} \left[\sin^{-1}\left(\frac{a}{c} \right) - \left(\frac{a}{c} \right) \sqrt{1 - \frac{a^2}{c^2}} \right] \right\} \quad (3.55)$$

with the ratio a/c determined by

$$\ln\left(\frac{c}{a} \right) - \frac{\kappa_T \eta E_0 \alpha_0 \Delta T}{2 \left[\beta_0 \sigma_Y^0 + \kappa_L (L_{ssy}^0 / L_0)^2 \sigma_L^1 \right]} \left(1 - \frac{a^2}{c^2} \right) = \frac{\pi}{8a} \left(\frac{K_c^0}{\beta_0 \sigma_Y^0 + \kappa_L (L_{ssy}^0 / L_0)^2 \sigma_L^1} \right)^2 \quad (3.56)$$

where the parameter κ_T is calibrated under the localized heating conditions, L_0 and L_{ssy}^0 are given in Eqs. (3.25) and (3.26), i.e.,

$$L_{ssy} = \frac{\pi}{8} \left(\frac{K_c^0}{\beta_0 \sigma_Y^0} \right)^2 \quad (3.57)$$

$$L = a \left\{ \exp\left[\frac{\pi}{8a} \left(\frac{K_c^0}{\beta_0 \sigma_Y^0} \right)^2 \right] - 1 \right\} \quad (3.58)$$

and σ_L^1 is given by

$$\sigma_L^1 = \frac{E_1 \xi^2}{12(1 - v_1^2)} \left(\frac{t}{a} \right)^2 \quad (3.59)$$

The parameter ξ in Eq. (3.59) satisfies the following nonlinear equation

$$\xi = F(\xi) \quad (3.60)$$

where $F(\xi)$ is given by

66

$$F(\xi) = \frac{2a}{t}\left(3 + \frac{\xi^2}{2} - \frac{9\xi}{4\tanh(\xi)} - \frac{3\xi^2}{4\sinh^2(\xi)}\right)^{1/8}\left[\frac{3\left(1-v_1^2\right)}{2E_1}\right]^{1/4}$$

$$\times\left(\frac{2t}{\pi R}\beta_0\sigma_Y^0 F_1(\lambda)\left\{\cos^{-1}\left(\frac{a}{c}\right) + \frac{\eta E_0 \alpha_0 \Delta T}{2\beta_0\sigma_Y^0 F_1(\lambda)}\left[\sin^{-1}\left(\frac{a}{c}\right) - \left(\frac{a}{c}\right)\sqrt{1-\frac{a^2}{c^2}}\right]\right\}\right)^{1/4} \quad (3.61)$$

It is clear that ξ and a/c satisfy the coupled equations (3.56) – (3.61). To simplify the analysis, the ratio a/c in Eq. (3.61) is first determined using Eq. (3.51) for small deflection. The coupling effect is absorbed in the calibrated parameter κ_L. ξ and σ_L^1 are then evaluated from Eqs. (3.59) – (3.61). Eqs. (3.55) and (3.56) are finally used to determine the burst pressure. Note that the modulus and Poisson's ratio are taken at the high temperature in Eq. (3.59). This is because large deflection mainly occurs in the heated zone.

As no test data for burst pressure under the high temperature conditions is available, the burst pressures are tentatively calculated for the four duplex steel cylinders for a temperature rise of $\Delta T=1000^\circ C$. The material properties of the steel at the room temperature are listed in Table 3.4 and the estimated properties at $1000^\circ C$ are listed in Table 3.5.

The pressure results are listed in Table 3.7. The parameter κ_L for large deflection is chosen as 1.6 and κ_T for thermal stresses is chosen as 1.0 in the calculations. Note that κ_L may take different values for room and high temperatures. It can be seen that the burst pressure is most increased by the consideration of the thermal stress and large deflection for the cylinder with the longest crack. For the cylinder with the shortest crack, however, the effect of thermal stress and large deflection may be neglected for the κ_L and κ_T values selected.

Table 3.7 Burst pressure results ($\kappa_L=1.6$, $\kappa_T=1.0$, $K_c = 392$ MPa-m$^{1/2}$)

Specimen	Diameter (mm)	Crack Length $2a$ (mm)	P_{MAX} (MPa) (room temperature, small deflection)	P_{MAX} (MPa) ($\Delta T = 1000^\circ C$, small deflection)	P_{MAX} (MPa) (room temperature, large deflection)	P_{MAX} (MPa) ($\Delta T = 1000^\circ C$, large deflection)
1	254 (10 in)	120	1.75	1.84	1.85	1.97
2	254 (10 in)	90	2.39	2.45	2.47	2.55
3	254 (10 in)	60	3.50	3.53	3.52	3.55
4	254 (10 in)	30	5.63	5.64	5.63	5.64

6. Crack Turning Problem

As stated in Section 4, when a thin-walled cylinder is subjected to localized heating, fracture may occur along the axial direction or along the boundary between the heated and room temperature zones. In both cases, the fracture is initiated within the heated zone as an axial crack. While Section 4 studies the burst pressure associated with crack extension in the axial direction, this section focuses on the crack deflection (turning) problem. Due to the difficulties in crack kinking analyses of shell structures, we follow the early DL models by first considering a cracked flat plate and then modifying the flat plate result with the so-called M correction factor. The analyses are tentative as the crack turning criterion is based on the linear elastic fracture mechanics theory.

6.1 Crack Deflection in Flat Plate

Consider an infinite plate with a crack subjected to mode I loading, as shown in Fig. 3.12. The stress intensity factor at the crack tip is K_I. The crack will grow along the original direction provided the material is homogeneous and isotropic. When the material is subjected to localized heating, its properties become position and orientation dependent because material properties are in general temperature-dependent. In this case, the crack may deflect even under symmetric mode I loading conditions. To study the crack deflection when the crack tip is at the boundary between the heated and room temperature zones, we consider a small kink along the heated zone boundary (perpendicular to the original crack orientation) at the main crack tip, as shown in Fig. 3.13. The stress intensity factors at the kink tip, k_I and k_{II}, can be expressed in terms of K_I at the main crack tip as follows (Murakami et al., 1987)

$$k_I = 0.372 K_I$$
$$k_{II} = 0.348 K_I \qquad (3.62)$$

Here the influence of the temperature-dependence of Young's modulus on k_I and k_{II} is ignored. We assume that the crack deflection occurs within the heated zone along the boundary. The energy release rate of the crack deflection is thus

$$G_{df} = \frac{1}{E_1}\left(k_I^2 + k_{II}^2\right)$$
$$= \frac{0.259}{E_1} K_I^2 \qquad (3.63)$$

where E_1 is Young's modulus in the heated zone. Note that the temperature-dependence of Young's modulus is considered in calculating the energy release rate.
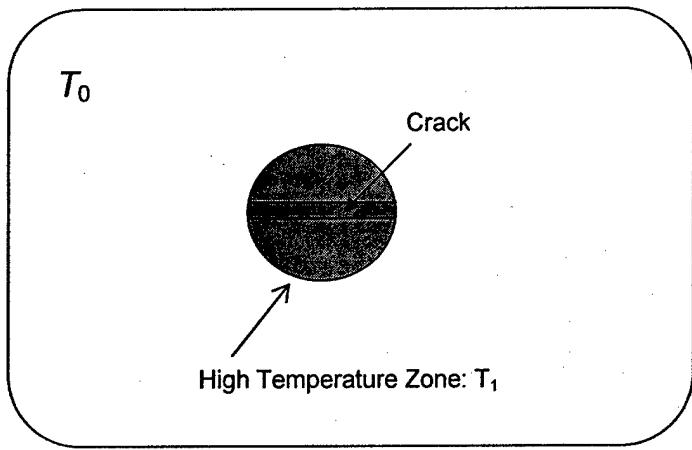
Fig. 3.12 An infinite plate with a crack subjected to localized heating

The energy release rate for the crack growth into the room temperature zone in the original direction is simply

$$G_{sf} = \frac{1}{E_0} K_I^2 \qquad (3.64)$$

where E_0 is Young's modulus in the room temperature zone. The crack deflection condition can thus be expressed as

$$\frac{G_{df}}{G_c^1} > \frac{G_{sf}}{G_c^0} \qquad (3.65)$$

where G_c^1 and G_c^0 are the critical energy release rates in the heated and room temperature zones, respectively. Substituting Eqs. (3.63) and (3.64) into the inequality (3.65) and considering

$$G_c^0 = \frac{1}{E_0} \left(K_c^0 \right)^2$$

$$G_c^1 = \frac{1}{E_1} \left(K_c^1 \right)^2 \qquad (3.66)$$

where K_c^0 and K_c^1 are the fracture toughness in the room and heated temperature zones, respectively, we have

$$\frac{K_c^1}{K_c^0} < \sqrt{0.259} = 0.509 \tag{3.67}$$

Here the effect of Mode II toughness on G_c^1 in Eq. (3.66) is ignored. Inequality (3.67) is obtained for a cracked plate under linear elastic conditions. Because no applied stress intensity factor is involved, it may also apply to the cracked cylinders. Inequality (3.67) may be used under elastic-plastic conditions if K_c^0 and K_c^1 are understood to represent the effective values with plasticity corrections.
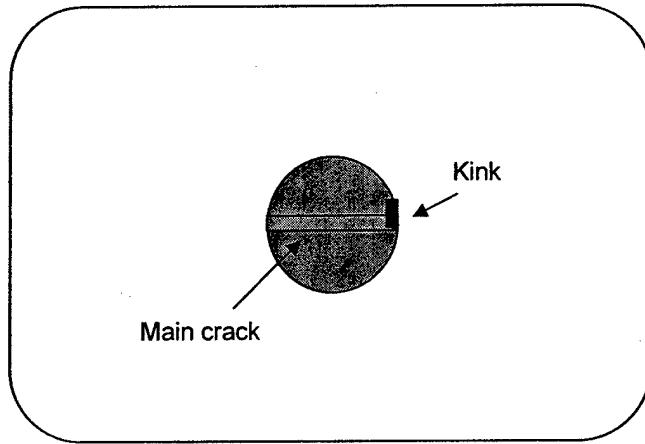
Fig. 3.13 A small kink crack at the main crack tip

6.2 Failure Hoop Stress and Burst Pressure

If the crack grows unstably along the original direction, i.e., condition (3.67) is not satisfied, the failure hoop stress and burst pressure can be calculated from Eqs. (3.53) and (3.54), respectively, i.e.,

$$\sigma_H = \frac{2}{\pi} \beta_0 \sigma_Y^0 F_1(\lambda) \left\{ \cos^{-1}\left(\frac{a}{c}\right) + \frac{\kappa_T \eta E_0 \alpha_0 \Delta T}{2\beta_0 \sigma_Y^0} \left[\sin^{-1}\left(\frac{a}{c}\right) - \left(\frac{a}{c}\right)\sqrt{1 - \frac{a^2}{c^2}} \right] \right\} \tag{3.68}$$

$$p_{\max} = \frac{2t}{\pi R} \beta_0 \sigma_Y^0 F_1(\lambda) \left\{ \cos^{-1}\left(\frac{a}{c}\right) + \frac{\kappa_T \eta E_0 \alpha_0 \Delta T}{2\beta_0 \sigma_Y^0} \left[\sin^{-1}\left(\frac{a}{c}\right) - \left(\frac{a}{c}\right)\sqrt{1 - \frac{a^2}{c^2}} \right] \right\} \tag{3.69}$$

where the ratio a/c is determined in Eq. (3.51), i.e.,

$$\ln\left(\frac{c}{a}\right) - \frac{\kappa_T \eta E_0 \alpha_0 \Delta T}{2\beta_0 \sigma_Y^0}\left(1 - \frac{a^2}{c^2}\right) = \frac{\pi}{8a}\left(\frac{K_c^0}{\beta_0 \sigma_Y^0}\right)^2 \tag{3.70}$$

The script '0' in Eqs. (3.68) - (3.70) stands for the properties in the room temperature zone. If the condition (3.67) is satisfied, the crack will grow along the boundary between the heated and room temperature zones. Now the failure hoop stress and the burst pressure may be calculated from

$$G_{df} = \frac{0.259}{E_1} K_I^2 = \frac{\left(K_c^1\right)^2}{E_1} \tag{3.71}$$

Note that K_I in the above equation is referred to the main crack tip. K_I may be described by K_{eff} in the DL model for crack extension in the axial direction for the first order approximation. The failure condition is thus obtained as

$$K_{eff}^2 = \frac{\left(K_c^1\right)^2}{0.259} \tag{3.72}$$

The plasticity corrected effective stress intensity factor, K_{eff}, is defined based on the strip plastic zone model as follows

$$K_{eff} = \sqrt{E_0 \beta_0 \sigma_Y^0 \delta_{tip}} \tag{3.73}$$

Using Eqs. (3.73) and (3.45), Eq. (3.72) can be written as

$$E_0 \beta_0 \sigma_Y^0 \delta_{tip} = \frac{1}{0.259}\left(K_c^1\right)^2 \tag{3.74}$$

Now the failure hoop stress and the burst pressure are still given by Eqs. (3.68) and (3.69), respectively, but with ratio a/c determined by

$$\ln\left(\frac{c}{a}\right) - \frac{\kappa_T E_0 \alpha_0 \Delta T}{2\beta_0 \sigma_Y^0}\left(1 - \frac{a^2}{c^2}\right) = \frac{\pi}{8a}\left(\frac{K_c^1}{0.509\beta_0 \sigma_Y^0}\right)^2 \tag{3.75}$$

6.3 Numerical Results

Whether the crack will deflect or not is first checked using the inequality (3.67). The burst pressures are then calculated for the four tested (tested under constant temperature) steel cylinders using Eqs. (3.68) - (3.70) (no crack deflection) or Eqs. (3.68), (3.69) and (3.75) (crack deflection) for a temperature rise of $\Delta T = 1000°C$. The material

71

properties of the steel at the room temperature are listed in Table 3.4. While the estimated values of Young's modulus, Poisson's ratio and the CTE at 1000°C are listed in Table 3.5, two fracture toughness values of 180 and 300 MPa-m$^{1/2}$ are assumed in this section and are listed in Table 3.8. The two values correspond to crack deflection and straight crack extension, respectively.

Table 3.8 Material properties of the steel at 1000°C

Yield Strength (MPa)	Ultimate Strength (MPa)	Hardening exponent	Young's modulus (GPa)	Poisson's ratio)	Thermal expansion (10^{-6} °C^{-1})	Toughness (K_c) (MPa-m$^{1/2}$)
			110	0.3	20	180, 300

First consider the case of $K_c^1 = 300$ MPa. Now $K_c^1 / K_c^0 = 0.77$ and the inequality (3.67) is not satisfied. Hence, the crack will extend from the high temperature region into the room temperature zone in the original axial direction. The burst pressure is now calculated using (3.68) - (3.70) and the results are listed in Table 3.9, which are the same as those listed in Table 5.6. It can be seen that the burst pressure is slightly increased by the consideration of the thermal stress.

Next consider the case of $K_c^1 = 180$ MPa. Now $K_c^1 / K_c^0 = 0.46$ and the inequality (3.67) is satisfied. Hence, the crack will turn into the direction of the boundary between the high temperature region and the room temperature zone. The burst pressure is now calculated using (3.68), (3.69) and (3.75) and the results are listed in Table 3.9. It is noted that for the K_c^1 selected, the burst pressure by considering crack turning remains almost the same as that without consideration of crack turning. This is because the pressure difference between the self-similar crack extension and crack turning is due to the terms in the right-hand sides of Eqs. (3.70) and (3.75) in the current model. $K_c^1 = 0.51 K_c^0$ represents a critical point at which the burst pressures from the two crack extension patterns are the same. If K_c^1 is smaller than and close to $0.51 K_c^0$, the pressure difference will be insignificant.

Table 3.9 Burst pressure results (small deflection)

Specimen	Diameter (mm)	Crack Length $2a$ (mm)	P$_{MAX}$ (MPa) (room temperature)	P$_{MAX}$ (MPa) ($\Delta T = 1000$°C, no crack turning)	P$_{MAX}$ (MPa) ($\Delta T = 1000$°C, crack turning)
1	254 (10 in)	120	1.75	1.84	1.78
2	254 (10 in)	90	2.39	2.45	2.40
3	254 (10 in)	60	3.50	3.53	3.48
4	254 (10 in)	30	5.63	5.64	5.63

7. Burst Pressures for Aluminum Cylinders

The burst pressures are also calculated for the four aluminum (Al 2014-T6) cylinders with a thickness of 3.175 mm using Eqs. (3.15) and (3.54) under both room and high temperature conditions. Table 3.10 lists the room temperature material properties for the aluminum. The toughness K_c is calculated using the test results of center cracked specimens and Irwin's formula with plasticity corrections. For cracks perpendicular to the grain direction (LT), test results from two specimens yield a K_c of 73 MPa-m$^{1/2}$. For cracks parallel to the grain direction (TL), the value of K_c is calculated as 57 MPa-m$^{1/2}$ from the test results. In the present calculations, we only consider LT cracks and a K_c of 81 MPa-m$^{1/2}$ is used, which results in burst pressures in agreement with the CTOA simulations.

Table 3.10 Material properties of Al 2014-T6 (room temperature)

Yield Strength (MPa)	Ultimate Strength (MPa)	Hardening exponent	Young's modulus (GPa)	Poisson's ratio	K_c (MPa-m$^{1/2}$) (LT)
420	460	0.03	72	0.33	73, 81

The burst pressure results for small deflections are listed in Table 3.11. It can be seen that with the selected K_c of 81 MPa-m$^{1/2}$, the predicted burst pressures of the DL model agree well with those obtained from the finite element simulations using the CTOA criterion except for the cylinder with the longest crack (140 mm).

Table 3.11 Burst pressures for Al 2014-T6 cylinders (small deflection, $K_c = 81$ MPa-m$^{1/2}$)

Specimen	Diameter (mm)	Crack Length $2a$ (mm)	P_{MAX} (MPa) (CTOA, LT)	P_{MAX} (MPa) (LT, $K_c = 81$ MPa-m$^{1/2}$)	λ
1	254	40	4.62	4.69	1.8
2	254	80	2.34	2.28	3.6
3	254	100	1.85	1.73	4.5
4	254	140	1.30	1.12	6.3

The burst pressure considering large deflection effects is also tentatively calculated and the results are listed in Table 3.12. The parameter κ_L in Eq. (3.28) is first selected as 7.5 (the value for the duplex steel cylinders) and K_c is 81 MPa-m$^{1/2}$. It can be seen from the table that the burst pressure is only slightly increased by considering the large deflection effect. The parameter κ_L, of course, needs further calibration for the aluminum cylinders in the future.

73

Table 3.12 Burst pressures for Al 2014-T6 cylinders (large deflection, $K_c = 81$ MPa-m$^{\frac{1}{2}}$)

Specimen	Diameter (mm)	Crack Length $2a$ (mm)	P_{MAX} (MPa) (small deflection)	P_{MAX} (MPa) (large deflection)	λ
1	254	40	4.69	4.74	1.8
2	254	80	2.28	2.36	3.6
3	254	100	1.73	1.79	4.5
4	254	140	1.12	1.15	6.3

The material properties for the aluminum at 400°C are listed in Table 3.13. The fracture toughness data at high temperatures is not used in the current DL model, and hence is not listed in the table. The room temperature CTE (22.3×10^{-6} °C^{-1}), however, is needed in the calculation of high temperature burst pressure.

Table 3.13 Material properties of Al 2014-T6 (400°C)

Yield Strength (MPa)	Ultimate Strength (MPa)	Hardening exponent	Young's modulus (GPa)	Poisson's ratio	Thermal expansion (10^{-6} °C^{-1})	K_c (MPa-m$^{1/2}$) (LT)
25	25	0.0	33	0.33	24.6	

The pressure results for the aluminum cylinders subjected to localized heating are calculated using Eqs. (3.51) and (3.54) with a room temperature toughness $K_c = 81$ MPa-m$^{\frac{1}{2}}$. The correction coefficient κ_T for the thermal stress is chosen as 0.3. The results are listed in Table 3.14. It is noted that in using Eqs. (3.51) and (3.54), if the Mises effective stress induced by the thermal stresses exceeds the material yield stress at the high temperature, the thermal stress is reduced so that the Mises stress is equal to the yield stress. It is observed from the table that with the selected correction coefficient $\kappa_T = 0.3$, the predicted high temperature burst pressures of the DL model are in reasonable agreement with those from the CTOA simulations. It is pointed out that in the calculations based on the CTOA criterion a temperature transition zone is present (see Fig. 3.14a) which is more realistic for modeling the temperature field. In the simple DL model, however, no such a temperature transition zone is considered (Fig. 3.14b), which may explain the bigger deviation of the DL model prediction from the CTOA simulation for the shortest crack case where the temperature transition zone plays a more important role at the specified temperature of 400 °C.

Table 3.14 Burst pressures for Al 2014-T6 cylinders (400 °C)

Specimen	Diameter (mm)	Crack Length $2a$ (mm)	P_{MAX} (MPa) (CTOA, 400 °C^{-1})	P_{MAX} (MPa) (room temperature)	P_{MAX} (MPa) (400 °C^{-1})	λ
1	254	40	4.07	4.69	4.73	1.8
2	254	80	2.32	2.28	2.32	3.6
3	254	100	1.86	1.73	1.77	4.5
4	254	140	1.35	1.12	1.15	6.3

To further explore the applicability of the DL model for the smaller hot spot case, burst pressures for the cylinder with the shortest crack (40 mm) under different temperatures in the hot spot are calculated and the results are listed in Table 3.15. It can be seen that except for the 400 °C case, the DL model predictions agree well with the CTOA simulations for all other three temperature cases wherein the temperature transition effects may not be very significant.

Table 3.15 Burst pressures for Al 2014-T6 cylinders (40 mm crack)

Temperature (°C)	Diameter (mm)	P_{MAX} (MPa) (CTOA)	P_{MAX} (MPa) (room temperature)	P_{MAX} (MPa) (high temperature)	λ
100	254	4.81	4.69	4.83	1.8
200	254	4.77	4.69	4.95	3.6
300	254	4.66	4.69	4.87	4.5
400	254	4.07	4.69	4.73	6.3

T_0 (room temperature)

T_0 (room temperature)


T_4

T_3

T_2

T_1

2a

2a

(a)

(b)
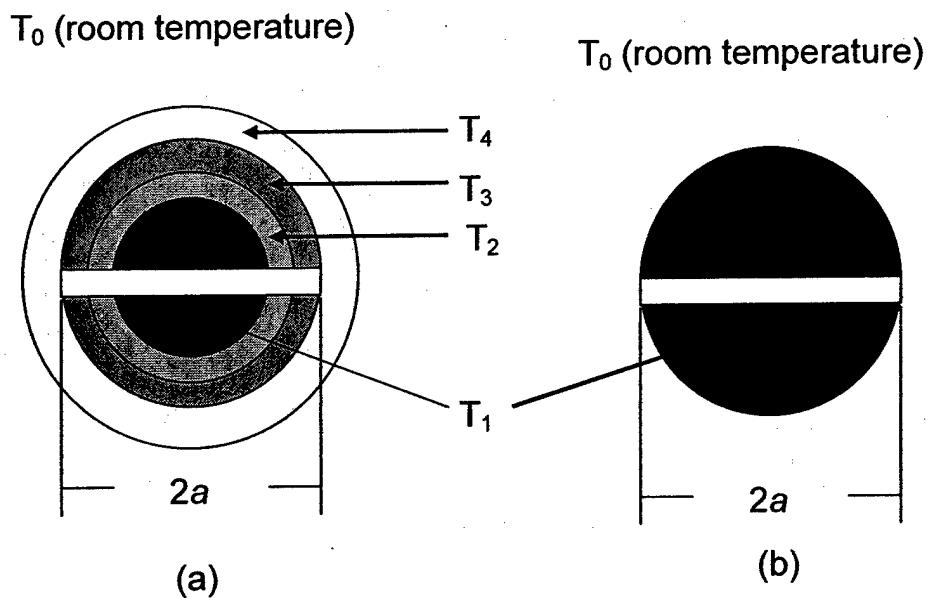
Fig. 3.14 (a) Hot spot and the crack with the temperature transition zone in the CTOA simulations; (b) Hot spot without temperature transition in the DL model

75

8. Concluding Remarks

The refined DL model (Sun et al., 2003) has been extended to predict failure of pressurized thin-walled cylinders undergoing large deflection along the crack surface and subjected to localized heating. In the present modification to the DL model to include large deflection effects, the membrane stress induced by the large deflection is approximately calculated and incorporated in the burst pressure formula with a free parameter κ_L that needs to be calibrated by matching the DL model prediction with the CTOA simulation result (large deformation). It is found that the burst pressure predictions of the DL model agree with the CTOA simulation results, as well as the test data with a single calibrated value of κ_L for the cylinder with the longest crack length and the DL model predictions are improved by considering the large deflection effect.

To include the localized heating effect into the DL model, the thermal stresses are first calculated for the flat plate case. A correction factor is then introduced to approximately obtain the thermal stress in the cylinder with a correction coefficient κ_T to be calibrated by CTOA simulation results. When the crack length is equal to the diameter of the heated zone and fracture occurs along the axial direction, the effect of the thermal stress on the crack opening displacement is included in the DL model. The burst pressure is tentatively calculated for the four tested steel cylinders (tested under constant temperature) and it appears that while the burst pressure is slightly increased by the consideration of the temperature effect for cylinders with longer cracks, it is not sensitive to the heating condition for cylinders with shorter cracks.

The burst pressures for the aluminum cylinders subjected to localized heating are also calculated and the results are compared with the CTOA simulations. With a correction coefficient κ_T for the thermal stress chosen as 0.3, the predicted high temperature burst pressures of the DL model are in reasonable agreement with those from the CTOA simulations except for the cylinder with the smallest hot spot. The bigger deviation of the DL model prediction from the CTOA simulation for this case may be due to the fact that the temperature transition zone is considered in the CTOA simulations, which plays a more important role at the specified temperature of 400 °C. In the simple DL model, however, no such a temperature transition zone is considered.

When an axially cracked cylinder is subjected to localized heating, the crack may also deflect (turn) along the boundary between the heated and room temperature zones. A simple crack deflection criterion is proposed based on the crack kink theory in LEFM, which shows that $K_c^1 = 0.51 K_c^0$ represents a critical point at which the burst pressures from the two crack extension patterns are the same. If K_c^1 is smaller than and close to $0.51 K_c^0$, the pressure difference between the two crack extension patterns will be insignificant.

References

1. Anderson, R. B. and Sullivan, T. L., 1966. Fracture mechanics of through-cracked cylindrical pressure vessels, NASA TN D-3252.
2. Anderson, T. L., 1995. *Fracture Mechanics*, 2nd Edition, CRC Press, Boca Raton.
3. Burdekin, F. M. and Stone, D. E. W., 1966. The crack opening displacement approach to fracture mechanics in yielding materials, *Journal of Strain Analysis*, Vol. 1, pp. 145-153.
4. Duffy, A. R., McClure, G. M., Eiber, R. J. and Maxey, W. A., 1965. Studies of hydrostatic test levels and defect behavior, Symposium on Line Pipe Research, American Gas Association, New York.
5. Dugdale, D. S., 1960, Yielding of steel sheets containing slits, *Journal of the Mechanics and Physics of Solids*, Vol. 8, pp. 100-104.
6. Erdogan, F. and Ratwani, M., 1972. Plasticity and the crack opening displacement in shells, *International Journal of Fracture Mechanics*, Vol. 8, pp. 413-426.
7. Folias, E. S., 1965. An axial crack in a pressurized cylindrical shell, *International Journal of Fracture Mechanics*, Vol. 1, pp. 104-113.
8. Hahn, G. T., Sarrate, M. and Rosenfield, A. R., 1969. Criteria for crack extension in cylindrical pressure vessels, *International Journal of Fracture Mechanics*, Vol. 5., pp. 187-210.
9. Kiefner, J. F., Maxey, W. A., Eiber, R. J. and Duffy, A. R., 1973. Failure stress levels of flaws in pressurized cylinders, in *Progress in Flaw Growth and Fracture Toughness Testing*, ASTM STP 536, pp. 461-481, American Society for Testing and Materials, Philadelphia.
10. Murakami, Y. (Editor-in-Chief), 1987, *Stress Intensity Factors Handbook*, Vol. 1, Pergamon Press, Oxford.
11. Peters, R. W. and Kuhn, P., 1957. Bursting strength of unstiffened pressure cylinder with slits, NASA TN 3993.
12. Rose, C. A., Young, R. D. and Starnes, J. H., 1999, Nonlinear local bending response and bulging factors for longitudinal cracks in pressurized cylindrical shells, AIAA-99-1412, American Institute of Aeronautics and Astronautics.
13. Sun, C. T., Jin, Z.-H. and Rangarajan, B., 2003. Prediction of ductile fracture in thin-walled cylinders under internal pressure, Final Report to Ball Aerospace & Technology and Air Force Research Laboratory (AFRL/DELE).
14. Timoshenko, S., 1940, *Theory of Plates and Shells*, McGraw-Hill Book Company, Inc., New York.